PURPOSE-LED
PUBLISHING™

**TOPICAL REVIEW • OPEN ACCESS**

# Hydride-based thermal energy storage

View the article online for updates and enhancements.

CrossMark

TOPICAL REVIEW

# Hydride-based thermal energy storage

Marcus Adams[1], Craig E Buckley[2] 🆔, Markus Busch[3], Robin Bunzel[4] 🆔, Michael Felderhoff[5],
Tae Wook Heo[6] 🆔, Terry D Humphries[2] 🆔, Torben R Jensen[7] 🆔, Julian Klug[4] 🆔, Karl H Klug[4],
Kasper T Møller[8] 🆔, Mark Paskevicius[2] 🆔, Stefan Peil[9], Kateryna Peinecke[5], Drew A Sheppard[5] 🆔,
Alastair D Stuart[1], Robert Urbanczyk[9] 🆔, Fei Wang[5], Gavin S Walker[1] 🆔, Brandon C Wood[6] 🆔,
Danny Weiss[4] 🆔 and David M Grant[1,*] 🆔

1  Advanced Materials Research, University of Nottingham, Nottingham, United Kingdom
2  Physics and Astronomy, Curtin University, GPO Box U1987, Perth, WA 6845, Australia
3  MBS GmbH, 46514 Schermbeck, Germany
4  Westfälische Hochschule, 45487 Gelsenkirchen, Germany
5  Max-Planck-Institut für Kohlenforschung, 45470 Mülheim an der Ruhr, Germany
6  Laboratory for Energy Applications for the Future (LEAF), Lawrence Livermore National Laboratory (LLNL), Livermore, CA 94550,
   United States of America
7  Department of Chemistry, Aarhus University, Aarhus, Denmark
8  Department of Biological and Chemical Engineering, Aarhus University, Aarhus, Denmark
9  Institut für Energie- und Umwelttechnik, 47229 Duisburg, Germany
*  Author to whom any correspondence should be addressed.

E-mail: david.grant@nottingham.ac.uk

## Abstract

The potential and research surrounding metal hydride (MH) based thermal energy storage is
discussed, focusing on next generation thermo-chemical energy storage (TCES) for concentrated
solar power. The site availability model to represent the reaction mechanisms of both the forward
and backward MH reaction is presented, where this model is extrapolated to a small pilot scale
reactor, detailing how a TCES could function/operate in a real-world setting using a conventional
shell & tube reactor approach. Further, the important parameter of effective thermal conductivity
is explored using an innovative multi-scale model, to providing extensive and relevant
experimental data useful for reactor and system design. Promising high temperature MH material
configurations may be tuned by either destabilisation, such as using additions to Ca and Sr based
hydrides, or by stabilisation, such as fluorine addition to NaH, $MgH_2$, or $NaMgH_3$. This versatile
thermodynamic tuning is discussed, including the challenges in accurately measuring the material
characteristics at elevated temperatures (500–700 °C). Attention to scale up is explored, including
generic design and prototype considerations, and an example of a novel pilot-scale pillow-plate
reactor currently in development; where materials used are discussed, overall tank design scope
and system integration.

## 1. Introduction

The scaling up of clean power is critical to prevent the disasters facing humanity if climate change is allowed
to accelerate. Harnessing solar energy is essential to achieve this, with available technologies such as solar
photovoltaics (PV) and solar thermal electricity. Solar PV is experiencing rapid growth, with world markets
estimated to add over 125 GW of capacity per year from 2021 to 2025. However, more effort is needed to
meet the International Energy Agency (IEA) target of over 7000 TWh by 2030. Solar thermal electricity, or
concentrated solar power (CSP), is experiencing a more modest growth, from 10 to 16 TWh from 2015 to
2019 and at this rate it will fall a long way short of the IEA target of 204 TWh by 2030. To stimulate the CSP
market, IEA recommends increasing research and reduce costs to attract the necessary investment [1]; in
particular, focusing on the value and potential of CSP thermal energy storage (TES).

TES is a significant advantage of CSP to combat fluctuating supplies of energy on the grid. Conversion of stored heat to work and ultimately to electrical energy can be accomplished in a Rankine cycle, in an Organic-Rankine cycle or Brayton process. Such an energy storage system that stores electricity in the form of thermal energy is called 'Brayton Battery' or 'Carnot Battery' [2, 3]. Water-based TES systems, such as closed-loop seasonal TESs, are widely used for the utilization of low-temperature heat [4]. However, these are of limited use for storing surplus energy such as medium- and high-temperature heat generated from industrial production processes. In contrast, the use of thermochemical energy storage (TCES) offers significantly larger share of usable work. In principle, TCES uses an endothermic chemical reaction to store heat and release it again during the exothermic reverse reaction.

For a suitable TES there must be sufficient solar energy in a CSP plant to make it viable. The key indicator for a suitable location of a CSP plant is direct normal irradiation (DNI). DNI is affected by cloud cover and when the DNI $< 2$ kWh m$^{-2}$ d$^{-1}$, the electricity generation is 0 [5]. Examples of suitable areas considering DNI only are the Atacama Desert in Chile (11 kWh m$^{-2}$ d$^{-1}$), south Namibia and western South Africa (8.8 kWh m$^{-2}$ d$^{-1}$), West Australia (8.2 kWh m$^{-2}$ d$^{-1}$), the Tibetan region of China (8 kWh m$^{-2}$ d$^{-1}$) and the Sinai Peninsula in Egypt (7.8 kWh m$^{-2}$ d$^{-1}$) [6].

Current state-of-the-art CSP plants operate between 290 °C and 565 °C using a 60/40 wt% blend of sodium and potassium nitrate, with the molten salt performing the role as heat transfer fluid (HTF) and a sensible thermal store, which is coupled to a Rankine steam cycle [7]. However, higher temperature CSP plants are more efficient, which helps to improve the economics and therefore competitiveness, with a typical temperature range between 600 °C and 750 °C, and a desired full night-time duration storage period (12–14 h) [8, 9].

To reach these higher temperatures chloride salts are required at $>700$ °C leading to corrosion issues and significant cost increase. For example a nitrate two-tank system has a cost of \$20–33 kWh$_{th}$$^{-1}$, while MgCl$_2$/KCl is estimated at \$58 kWh$_{th}$$^{-1}$, above the CSP-TES target of $<$\$15 kWh$_{th}$$^{-1}$ [9]. A design using ceramic particles as the heat transfer medium has also been proposed, with silos as storage. This design was estimated to exhibit storage costs of \$22 kWh$_{th}$$^{-1}$ and \$15 kWh$_{th}$$^{-1}$ for insulated steel tanks and firebrick tanks, respectively. The challenge with this route is not the thermal storage, but the design of the particle to CO$_2$ heat exchanger and system/unit development for a solid heat transfer medium [8, 9].

Utilising a higher energy density technology for TES offers the potential for smaller stores and less material, such as phase change materials (PCMs) and TCES. For example, a multi-tube heat exchanger utilising latent heat (chlorides) was estimated at \$39 kWh$_{th}$$^{-1}$, again above the CSP-TES target [9]. Of the three TES technologies (sensible heat, PCM and TCES) TCES has the lowest thermal exergy losses and the highest material energy density, offering potentially low cost. However, it is currently at the lowest technology readiness level, due to high complexity [10, 11].

Many TCES systems have been proposed and tested, from reversible steam methane reforming [12] reversible ammonia synthesis/cracking [13], reversible reactions involving metal oxides (including chemical looping), carbonates, hydroxides or sulphates and reversible metal hydrides (MHs) [10, 14–18].

There are several elements that are key for a successful TCES candidate. These are a suitable operating temperature, typically up to 565 °C (to be retrofitted to current plants) and between 600 °C and 750 °C (for future generation plants), reversibility and cyclability over 10 000 cycles, overall system cost and a small operating temperature gap between the forward and backward reaction (small reaction hysteresis).

For example, industrial ammonia synthesis occurs under an iron catalyst at 300–400 °C, while ammonia cracking under a Ruthenium based catalyst at approximately 700 °C [13]. A lithium amide catalyst has been proposed that can operate at 400 °C but long cycle life is still a concern [19]. This means the receiver can supply temperatures at approximately 700 °C, but the power block temperature is limited at 400 °C, demonstrating thermal exergy losses.

Metal oxides are an interesting competitive alternative due to oxygen being drawn from the air, removing gas storage. Again, oxide systems (such as Mn$_2$O$_3$/Mn$_3$O$_4$) suffer reaction hysteresis [10, 20], however, these can be negated through creating binary metal oxides such as Cu/(Cu + Mn), which exhibit faster kinetics and improved cycling stability [20]. Materials chosen usually involve Mn, Ba or Cu due to their lower cost and operate a charging temperature of greater than 900 °C [14].

Sulphate systems are high energy density (1500–3000 kJ kg$^{-1}$) and operate at high temperatures around 1000 °C but have significant corrosion challenges. Hydroxide systems (e.g. Ca/Sr/Ba) have been projected as an affordable TCES technology (\$17–30 kWh$_{th}$$^{-1}$) but these systems also suffer reaction hysteresis and capacity issues persist at higher cycles due to a carbonation side reaction [10].

MHs can operate at a wide range of target temperatures for solar power such as MgH$_2$ for parabolic trough plants operating between 300 °C and 400 °C [5] to more efficient solar power towers operating at higher temperatures such as 565 °C (e.g. Na/Mg based) and around 700 °C (e.g. Ca/Sr based) [15]. These examples are fully reversible with low reaction hysteresis, if the appropriate pressure swing (hydrogenation to

dehydrogenation) is adopted with hydrogen storage. For MH TCES materials, there is a significant advantage in being able to tune the properties to the temperatures required, utilising destabilisation or stabilisation techniques. This is particularly useful in finding competing solutions to the 700 °C range. For example, for the calcium hydride system, $\Delta H = 208$ kJ mol$^{-1}$ H$_2$. If based on this 'parent' system, adding aluminium destabilises the parent system, enabling an alternative reaction with $\Delta H = 83$ kJ mol$^{-1}$ H$_2$ [15].

Although the material energy density of MHs (not including H$_2$ storage) often exceeds metal carbonates and hydroxides, the natural occurrence of carbonates/hydroxides is a benefit considering cost, and the capability of handling the materials in air is another advantage. As such, metal carbonate systems have already been demonstrated in pilot plants on a MW$_{th}$ scale [21, 22]. However, the main challenge remains their energy capacity loss over multiple cycles [21, 23]. Sintering is a key obstacle and many ways have been explored to circumvent this [24–30]. Even promising solutions such as the CaCO$_3$-Al$_2$O$_3$ system, indicated the reactor configuration may promote sintering when scaled up to kg level [31].

One major aspect that must be considered is the storage of hydrogen gas that is released during the endothermic charging (hydrogen desorption) process of the thermal battery. Hydrogen can be stored in a closed or an open loop system. In a closed system, H$_2$ storage is exclusively sized for the CSP plant. In an open system, the H$_2$ storage is shared across multiple users, for instance, a large complex could entail a H$_2$ generation plant, ammonia synthesis, steel manufacture and a CSP plant, all sharing H$_2$ storage. Although hydrogen gas can be stored in canisters near room temperature, its volumetric density is low, even under high pressure. For instance, if 1 TJ of energy is to be stored by CaH$_2$, 238 tonnes of MH is required [15]. This would mean that over 129 000 m$^3$ (at standard temperature and pressure) of H$_2$ gas must be stored. Current options to store this H$_2$ include compression into vessels (above ground 250 bar US $450 kg$^{-1}$ H$_2$ [32]), underground caverns (salt US $1.6–5 kg$^{-1}$ H$_2$ or lined rock US $12–26 kg$^{-1}$ H$_2$ [32]), or sorption of H$_2$ by a low temperature metal hydride (LTMH) (such as NaAlH$_4$ at US $1400 kg$^{-1}$ H$_2$ based on 5.6 kg H$_2$ tank [33]). Another suggested method is to store H$_2$ within a magnesium hydride slurry system [34]. Each of these options have their advantages and disadvantages. Techno-economic assessment at the operating temperature case of 565 °C using various promising hydrides (e.g. MgH$_2$, Mg$_2$FeH$_6$, NaMgH$_3$, NaMgH$_2$F and NaH) with underground gas storage determined a competitive specific installed cost range from US $14–27 kWh$_{th}$$^{-1}$ [32].

At present, TES using high temperature MHs have only been demonstrated on a kilogram-scale on several of occasions [35–37]. The reasons for MH systems having difficulty to progress are due to technical bottlenecks, principally: kinetic modelling, materials, and reactor design. As such, this paper concentrates on addressing these three keys:

(a) Modelling thermal storage systems: Key to designing a practical thermal store is the importance of suf-ficiently modelling the reaction kinetics of MHs. Often, an empirical approach is adopted, combining established solid/gas models with various dimensionless pressure terms, however this approach is not readily transferrable with any considerable accuracy. Here, we have developed the site availability model (SAM) that improves on these deficiencies, and it is presented in section 2.1. Thermal transport properties are also essential, and in section 2.2 we present a mesoscopic modelling framework, which provides a use-ful computational tool for systematically investigating the relationship between complex microstructure and thermal transport properties of MHs.

(b) Materials selection and reactor design: Thermal measurements and vessel design are also critical to thermal store development. Approaches to thermodynamically tune MH candidate materials to match the requirements of a thermal store are explored in 3.1, while the challenges of measurements of thermo-dynamics, thermal conductivity and reactor design are detailed in sections 3.2–3.4.

(c) Scale-up: The development of an original scale up design is introduced in section 4, demonstrating a large-scale MH thermal store industrial prototype being developed in the 'HyHeatStore' project funded by European Union and state of North Rhine-Westphalia (NRW) in Germany. In this prototype, approxim-ately 350 kg of magnesium hydride is proposed to store about 200 kWh$_{th}$ in a temperature range between 370 °C and 400 °C.

## 2. Modelling hydride TCES systems

Models representing reaction kinetics for MHs are often specific to certain systems and operational conditions, and some models are effective for some materials, but not others. Models available in the literature do not sufficiently represent metal hydrogenation or hydride dehydrogenation across practical operating temperature and pressure ranges. As such, until now, no model has successfully represented a hydride suitable for CSP TES. A common approach is to combine established solid/gas kinetic models

[38–43] with dimensionless pressure terms [44] in an empirical fashion [45–50]. MH kinetics are a function of temperature, pressure, and heat transfer, and these three elements should be present in a rate law [51–53].

To improve the understanding of MH kinetics, the SAM was developed, whereby the model has shown promise at representing both magnesium hydrogenation and magnesium hydride dehydrogenation, a CSP candidate. The SAM is outlined here, and it is postulated that the SAM could be applied to higher temperature MH CSP candidates in the future. As proven from results at 0.2 g and at 154 g [54, 55], mass transfer considerations are not required using the SAM at this scale. This is considering both flow through porous media and mass transfer effects at a particle level. At small reactor sizes, the reaction rate is governed by the surface reaction front, rather than the transport of $H_2$ to/from the site. At larger reactor sizes, mass transport may have to be included. Regarding mass transfer effects at the particle level, it was shown that diffusion resistance of the hydride layer was inconsequential compared to surface resistance effects, in which the surface resistance is assumed where the Site Availability occurs [54].

Further, commercial sized MH reactors are severely inhibited by heat transfer issues, particularly driven by poor thermal conduction. As such, thermal conductivity of powders is an important parameter within MH kinetics, and a phase-field model that facilitates improved representation of the thermal conductivity is described in section 2.2.

### 2.1. Modelling hydrides kinetics using the SAMs

#### 2.1.1. Reaction kinetics

The SAM was validated for the hydrogenation of magnesium and the dehydrogenation of magnesium hydride at 0.2 g and 154 g samples using atomised Mg powder from SFM (Fluorsid Group) with an average particle size of 26 $\mu$m [54, 55]. The SAM is a surface-based model that expands on the theory of the Langmuir Adsorption Model (LAM), where a site can not only be vacant/occupied but also unavailable/available. Thus, it is possible to encounter a site at a certain time to be vacant, but unavailable for reaction. A certain time later that same site can be vacant and available for reaction, and subsequently, occupied. As the SAM is based on LAM, the key elements of the reaction rate are occurring at the surface, and thus the changing surface over time is included [54, 55]. The hydrogenation rate equation is based on assuming equation (2) as rate determining, with $\boldsymbol{H}$ = a mono-hydrogen or component $\boldsymbol{H}$, $\boldsymbol{M}$ = empty metal site and $\boldsymbol{H} \cdot \boldsymbol{M}$ = bound metal site

$$\frac{1}{2}H_2 \rightarrow \boldsymbol{H} \tag{1}$$

$$\boldsymbol{H} + \boldsymbol{M} \rightarrow \boldsymbol{H} \cdot \boldsymbol{M} \tag{2}$$

$$r_{H \cdot M} = \frac{dC_{H \cdot M}}{dt} = k_{e_s} \sigma_s C_T (1-\theta)^{\frac{5}{3}}. \tag{3}$$

The hydrogenation reaction rate ($r_{H \cdot M}$) is proportional to the sorption site availability ($\sigma_s$) and a 5/3 order rate equation governed by a shrinking core mechanism. The rate equations are based on the concentration of bound metal sites ($C_{H \cdot M}$) and limited by the total site concentration ($C_T$). Time is noted by $t$.

The dehydrogenation rate equation (7) is based on the following reaction mechanism, where equation (4) (step 1) is assumed rate determining and $\boldsymbol{M} \cdot \cdot \boldsymbol{H} \cdot \cdot \boldsymbol{M}$ is an idealised transition state

$$\boldsymbol{H} \cdot \boldsymbol{M} + \boldsymbol{M} \rightarrow \boldsymbol{M} \cdot \cdot \boldsymbol{H} \cdot \cdot \boldsymbol{M} \tag{4}$$

$$\boldsymbol{H} \cdot \boldsymbol{M} + \boldsymbol{M} \cdot \cdot \boldsymbol{H} \cdot \cdot \boldsymbol{M} \rightarrow H_2 + 3\boldsymbol{M} \tag{5}$$

$$2\boldsymbol{H} \cdot \boldsymbol{M} \rightarrow 2\boldsymbol{M} + H_2 \tag{6}$$
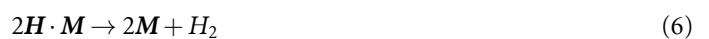
$$-r_{H \cdot M} = k_{e_D} \sigma_D C_T (1-\theta) \theta^{\frac{5}{3}} \left( k_f (1-\theta)^2 + 1 \right)^2. \tag{7}$$

The dehydrogenation rate ($-r_{H \cdot M}$) is governed by the desorption site availability ($\sigma_D$), an auto-catalytic reaction, where free metal sites act as the auto-catalyst, and particle fragmentation combined with a shrinking core, giving an overall effective expanding core for most of the reaction [55]. In strict theory terms, the site availability terms should not be greater than one. The normalised hydride fraction ($\theta$) is defined by (8)

$$\theta = \frac{x}{x_M} = \frac{C_{H \cdot M}}{C_T} = \frac{C_{H \cdot M}}{C_{ref} x_m}. \tag{8}$$

The maximum hydride fraction ($x_\mathrm{m}$) is the maximum hydrogen uptake for a single hydrogenation, which is related to the reference concentration ($C_\mathrm{ref}$) governed by the material's theoretical maximum (for example, with magnesium hydride this is taken as 7.66 wt%). Therefore, the total concentration and hydride fraction are $C_\mathrm{T} = C_\mathrm{ref}x_\mathrm{m}$ and $x = C_{H \cdot M}/C_\mathrm{ref}$ respectively.

For hydrogenation, the hydrogenation/sorption effective rate constant $k_{e_s} = A_{e_s}\exp\left(-E_{e_s}/\boldsymbol{R}T\right)$, with $A_{e_s}$ the effective hydrogenation pre-exponential factor and $E_{e_s}$ the effective hydrogenation activation energy. The sorption site availability is dependent on whether the system is at close or far from equilibrium [55]. For close to equilibrium conditions, $\sigma_\mathrm{s} = (P_\mathrm{g} - P_\mathrm{B})/P_\mathrm{B}$, ($P_\mathrm{g}$ = gas pressure) with the bound pressure $P_\mathrm{B}$ represented by (9)

$$P_B = \exp\left(\frac{\Delta_r H}{\boldsymbol{R}T} - \frac{\Delta_r S}{\boldsymbol{R}}\right)\left(1 - \frac{1}{y_1}\ln\left(\frac{1-\theta}{\theta}\right)\right). \tag{9}$$

Equation (9) requires $\theta > 0$ as an initial starting condition. $\boldsymbol{R}$, $T$, $\Delta_\mathrm{r}H$, $\Delta_\mathrm{r}S$ and $y_1$ are the universal gas constant, temperature, enthalpy of reaction, entropy of reaction and curve growth rate, respectively. Between practical temperature ranges, $y_1$ can be assumed a function of normalised hydride fraction only ($\theta$) and determined through regression to experimental PCI data. For the magnesium hydride system equation (10) was used (the $\alpha$-phase is ignored)

$$y_1 = -245.09\theta^4 + 310.95\theta^3 - 123.74\theta^2 - 12.268\theta + 73.943. \tag{10}$$

For dehydrogenation, the dehydrogenation effective rate constant $k_{e_\mathrm{D}} = A_{e_\mathrm{D}}\exp\left(-E_{e_\mathrm{D}}/\boldsymbol{R}T\right)$ (with $A_{e_\mathrm{D}}$ the effective dehydrogenation pre-exponential factor and $E_{e_\mathrm{D}}$ the effective dehydrogenation activation energy), and the desorption site availability $\sigma_\mathrm{D} = \left(P_\mathrm{B} - P_\mathrm{g}\right)/P_\mathrm{B}$. $P_\mathrm{B}$ is determined either using equation (9), or by the van't Hoff equation. It was found for dehydrogenation at high site availability driving force (i.e. $\sigma_\mathrm{D} \approx 0.8 - 1$, so the gas pressure is far from the hydrogen bound pressure), the van't Hoff equation (11) is sufficient

$$P_B = \exp\left(\frac{\Delta_\mathrm{r} H}{\boldsymbol{R}T} - \frac{\Delta_\mathrm{r} S}{\boldsymbol{R}}\right). \tag{11}$$

The fragmentation rate constant $k_f$ within the term $\left(k_f(1-\theta)^2 + 1\right)^2$ governs the extent of particle fragmentation. The fragmentation rate constant is a function of both over-pressure and temperature, where the relationship between over-pressure and $k_f$ was found to be linear within the pressures tested, and the temperature relationship was based on an Arrhenius type expression, with $A_f$ and $E_f$ the fragmentation pre-exponential factor and activation energy respectively [55].

*2.1.2. Energy balance*
The energy balance was assumed dominated by thermal conduction and the rate of temperature change is a function of the volumetric heat capacity (porous media),

$$\left(\rho c_{p_e}\right)_e \frac{\partial T}{\partial t} + \nabla \cdot \mathbf{q} = Q \tag{12}$$

$$\lambda_e = \lambda_s\left(1 - \varepsilon\right) + \lambda_g\varepsilon \tag{13}$$

$$\left(\rho c_{p_e}\right)_e = c_{p_g}\rho_g\varepsilon + c_{p_s}\rho_s\left(1 - \varepsilon\right) \tag{14}$$

where the duty of the reaction, $Q = r_{H \cdot M}\left(-\Delta_\mathrm{r}H\right)$ for hydrogenation, for example. $\mathbf{q}$ is the conductive heat flux vector ($\mathbf{q} = -\lambda_e\nabla T$). The volumetric specific heat $\left(\rho c_{p_e}\right)_e$ and effective thermal conductivity of the powder $\lambda_e$ are based on 'weight arithmetic mean' terms (equations (13) and (14)), where subscript $e$ is effective, $g$ is gas/fluid and $s$ is solid. $c_p$ is the specific heat capacity at constant pressure and the bed porosity is defined as $\varepsilon$. The equations were solved using COMSOL, a commerically available numerical solver. The hydrogen gas data values were taken from the COMSOL directory, and the solid data (porous matrix) values were assumed constant. The thermal conductivity was more sensitive than the heat capacity within equation (12) due to the dominance of conductive heat transfer. It is acceptable to assume a constant $\lambda_e$ when modelling an individual run if at high pressure (see figure 9), however $\lambda_e$ can change with cycles (see figure 10) so a more thorough approach would be to model across a range of $\lambda_e$, for example.

At higher temperatures (typically above 500 °C) radiative heat transfer will also need to be considered. However, equation (13) represents the effective thermal conductivity (ETC or $\lambda_e$) in rather simplistic terms, and in section 2.2 a more sophisticated approach is proposed.
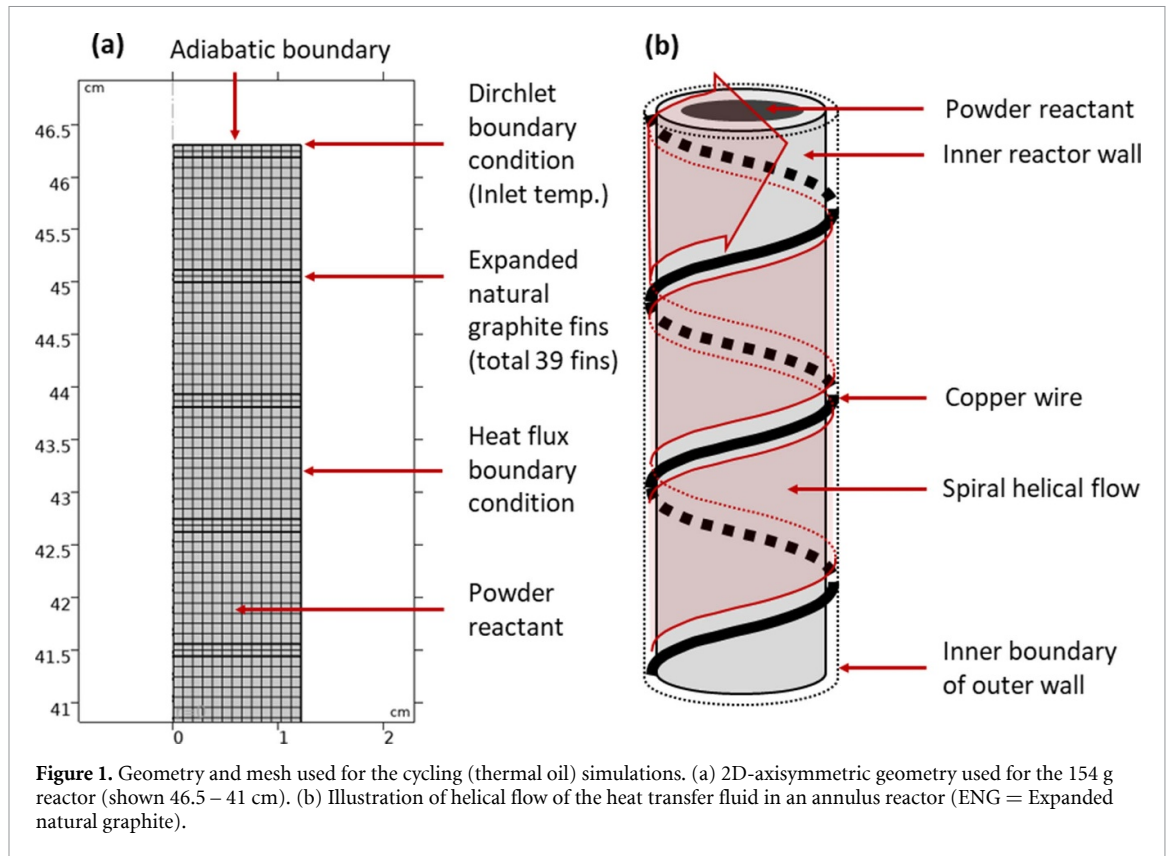
**Figure 1.** Geometry and mesh used for the cycling (thermal oil) simulations. (a) 2D-axisymmetric geometry used for the 154 g reactor (shown 46.5 – 41 cm). (b) Illustration of helical flow of the heat transfer fluid in an annulus reactor (ENG = Expanded natural graphite).

The heat of reaction used within the energy balance is assumed constant and is determined from thermodynamic/PCI measurements. The heat supplied/removed to the 154 g Mg reactor was tested in both electric heating and Marlotherm SH thermal oil configurations (figure 3).

*2.1.2.1. Modelling with thermal oil*
The reactor was a double pipe reactor where the powder was positioned in a central tube, and HTF flowed around the central tube in a helical direction (helical flow down an annulus). See figure 1 for visualisation. A mapped mesh was used in a 2D-axisymmetric geometry with the plane revolved around the centreline. The model ran the full reactor length ($L = 46$ cm) with thermal insulating boundaries at the top and bottom. The initial temperature was 300 °C across all domains with the initial reactant $H \cdot M$ concentration just above $0$ mol m$^{-3}$ for hydrogenation and at maximum for dehydrogenation. The volume to determine the concentration was the whole reaction domain.

To model the thermal oil temperature profile, equation (15) was assigned to the outer boundary,

$$\frac{\partial T_F}{\partial t} + c_{p_F}\dot{m}_F\frac{\partial T_F}{\partial z} = 2\pi R_i U(T - T_F) \tag{15}$$

with subscript $F$ denoting the HTF, $\dot{m}_F$ = HTF flow rate, $R_i$ = inner radius of the reactor bed (e.g. if the reactant was positioned inside a tube, $R_i$ is the inner radius of tube), $U$ = overall heat transfer coefficient and $z$ is the geometry length scale of the reactor (e.g. when $z = 0$ this is the reactor length ($L$) start point and the reactor end point is at $z = L$,). This was achieved using the Coefficient Form Boundary PDE COMSOL interface. A heat flux boundary was assigned in COMSOL as $-h_o(T - T_F)$, and a Dirchlet boundary condition was assigned at a corner point (inlet temperature). The convective heat transfer coefficient based on the outside of the tube ($h_o$) was calculated (within the Nusselt number) for helical flow down an annulus based on a numerical correlation determined by El Maakoul *et al* [56]

$$NuPr^{\frac{1}{3}} = 0.04572Re^{0.6098}(1 + B)^{7.565}. \tag{16}$$

In equation (16), $B$ is the baffle spacing, Nu = Nusselt number, Re = Reynolds number and Pr = Prandtl number. The hydraulic diameter was assumed to be a fully filled rectangular duct. The overall heat transfer coefficient ($U$) is based on the inside tube area of a single tube ($A_i$),

$$\frac{1}{U_i} = \frac{A_i}{h_o A_o} + \frac{x_w A_i}{\lambda_w A_w} + \frac{1}{h_{tc}} + \frac{x_i}{\lambda_{ee}} \approx \frac{d_i}{h_o d_H} + \frac{x_i}{\lambda_{ee}} \tag{17}$$

**Figure 2.** Geometry and mesh used for the activation (electric heating) simulations. (a) Base geometry showing the individual domains. (b) Same snapshot but illustrating the tetrahedral mesh. (c) Zoomed mesh of the interface between copper and steel walls.
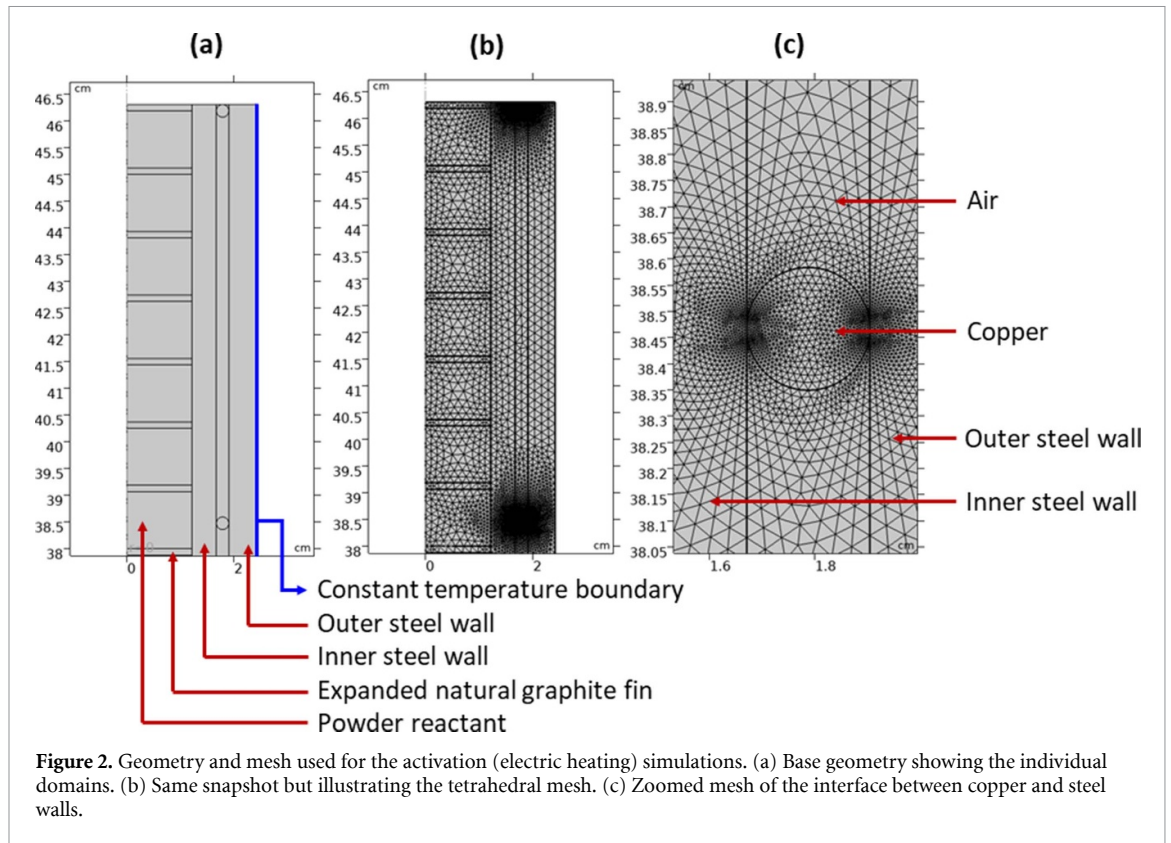
where $A_i/(h_oA_o)$ is the thermal resistance at the outside tube (subscript o), $(x_wA_i)/(\lambda_wA_w)$ is the thermal wall resistance (subscript w), $1/h_{tc}$ is the thermal contact resistance between powder and inside tube wall, and $x_i/\lambda_{ee}$ is the approximate powdered bed thermal resistance. $x$ is the length in the radial direction of the respective parameter, $A$ is area, $h$ is the transfer coefficient and $d$ is diameter (subscript $i$ is at the inside wall and $d_H$ is the hydraulic diameter). The effect of internal heat transfer architecture such as fins is included within the thermal conductivity, such that the equivalent ETC ($\lambda_{ee}$) is described as,

$$\lambda_{ee} = \varepsilon\lambda_f + (1-\varepsilon)(\lambda_{IHTA}\lambda_s).$$ (18)

As the wall and thermal contact resistance are omitted, and the powdered bed resistance is approximated, the accuracy of $U$ is reduced.

*2.1.2.2. Modelling with boundary electric heating*
To model the electric heating scenario, a separate geometry was adopted. The heater boundary was assumed to be at constant temperature, with thermal insulating boundaries at the top and bottom (figure 2(a)). A tetrahedral mesh was used across all domains with the helical copper wire approximated by circles, as shown in figures 2(b) and (c). The circle once revolved is a torus. In between the wires is an air domain (no fluid inside), with a steel domain either side. The geometry runs the length of the reactor. The initial temperature was 380 °C and the initial reactant $\boldsymbol{H} \cdot \boldsymbol{M}$ concentrations (either hydrogenation or dehydrogenation) were the same as described in section 2.1.2.1.

*2.1.3. Validating model*
The electric heating setup and the thermal oil circuit are shown in figure 3. The electric heating setup was used for magnesium activation. Figure 3(d) shows the reactor commissioned within the thermal oil circuit to validate the SAM. Diagrams of the hydrogen manifold and thermal oil circuit are shown in figure 4. The configuration allows operation in hydrogenation and dehydrogenation modes. For hydrogenation, the gas is supplied from bottles passing through a pressure regulator, through the flow meter, through the needle valve and then into the reactor. During dehydrogenation, the gas passes through the passive cooling loop, through the flow meters, through the needle valve and out to the vent line, either directly, or passing through the vacuum pump first. The temperature in the reactor was measured with three thermocouples, TC1, TC2 and TC3 and shown in figure 4. The average temperature profiles in figure 5 are an average of TC1, TC2 and TC3.
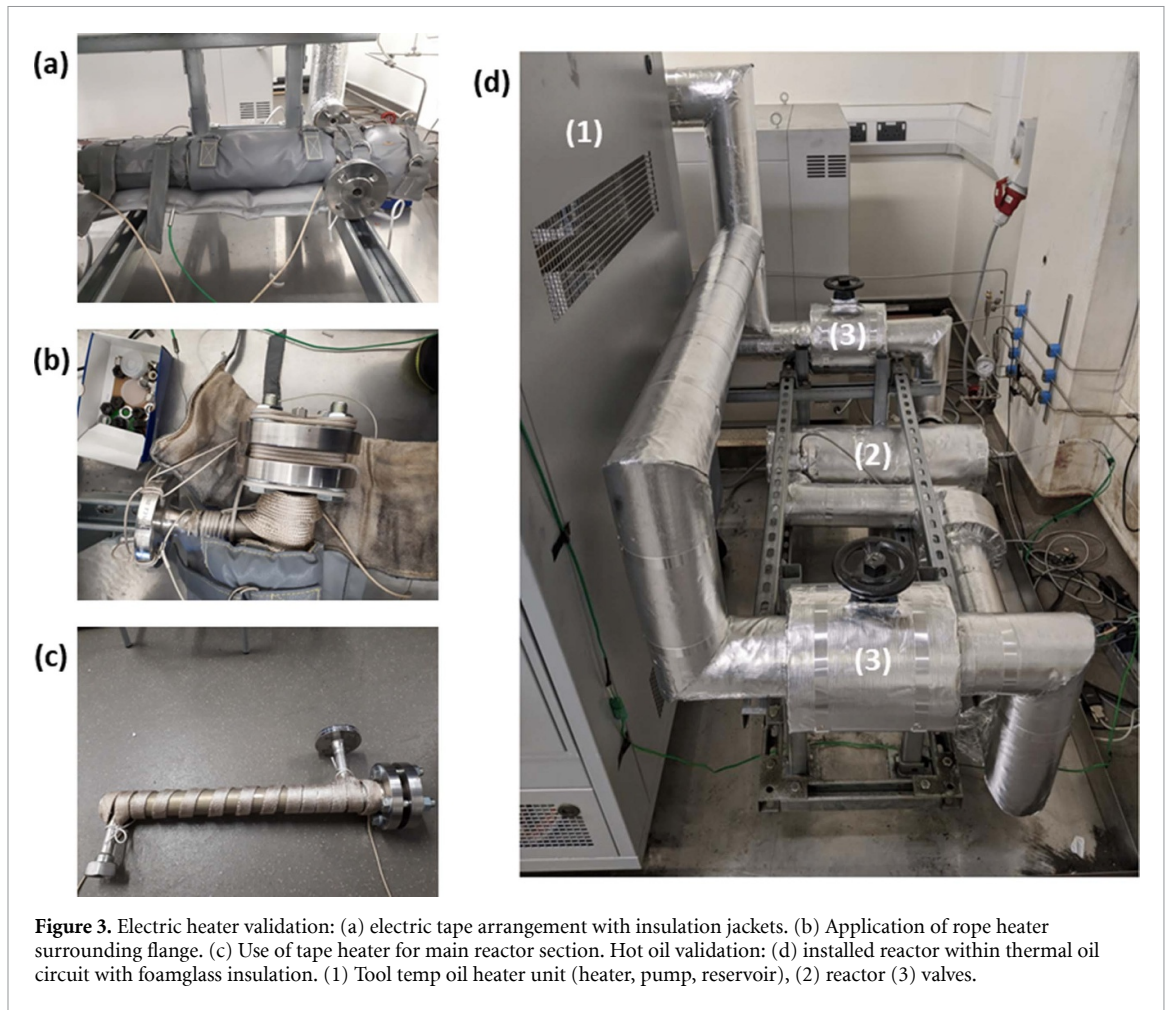
**Figure 3.** Electric heater validation: (a) electric tape arrangement with insulation jackets. (b) Application of rope heater surrounding flange. (c) Use of tape heater for main reactor section. Hot oil validation: (d) installed reactor within thermal oil circuit with foamglass insulation. (1) Tool temp oil heater unit (heater, pump, reservoir), (2) reactor (3) valves.
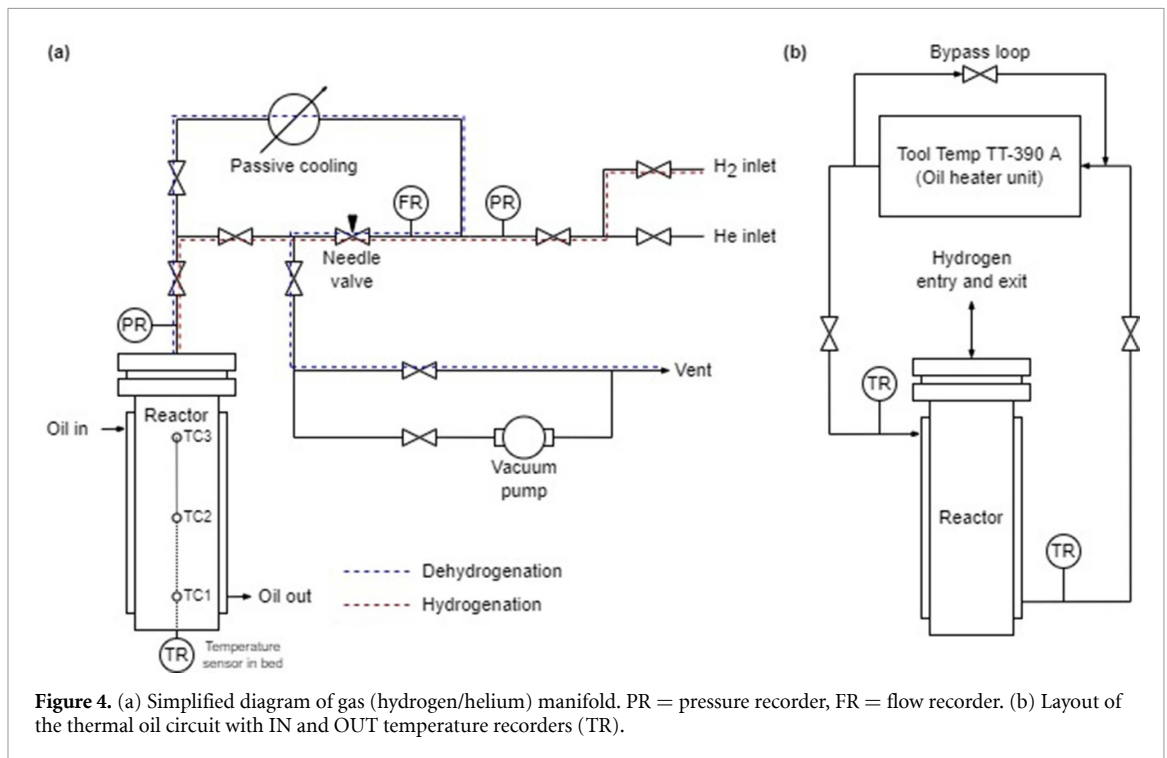


**Figure 4.** (a) Simplified diagram of gas (hydrogen/helium) manifold. PR = pressure recorder, FR = flow recorder. (b) Layout of the thermal oil circuit with IN and OUT temperature recorders (TR).

The results for testing the SAM to a 154 g magnesium reactor using this electric heating and thermal oil configuration is shown in figure 5. The SAM hydrogenation model uses equation (3) with the site availability as $\sigma_s = (P_g - P_B)/P_B$, and $P_B$ represented by equation (9). The SAM:ACR:F (Auto Catalytic
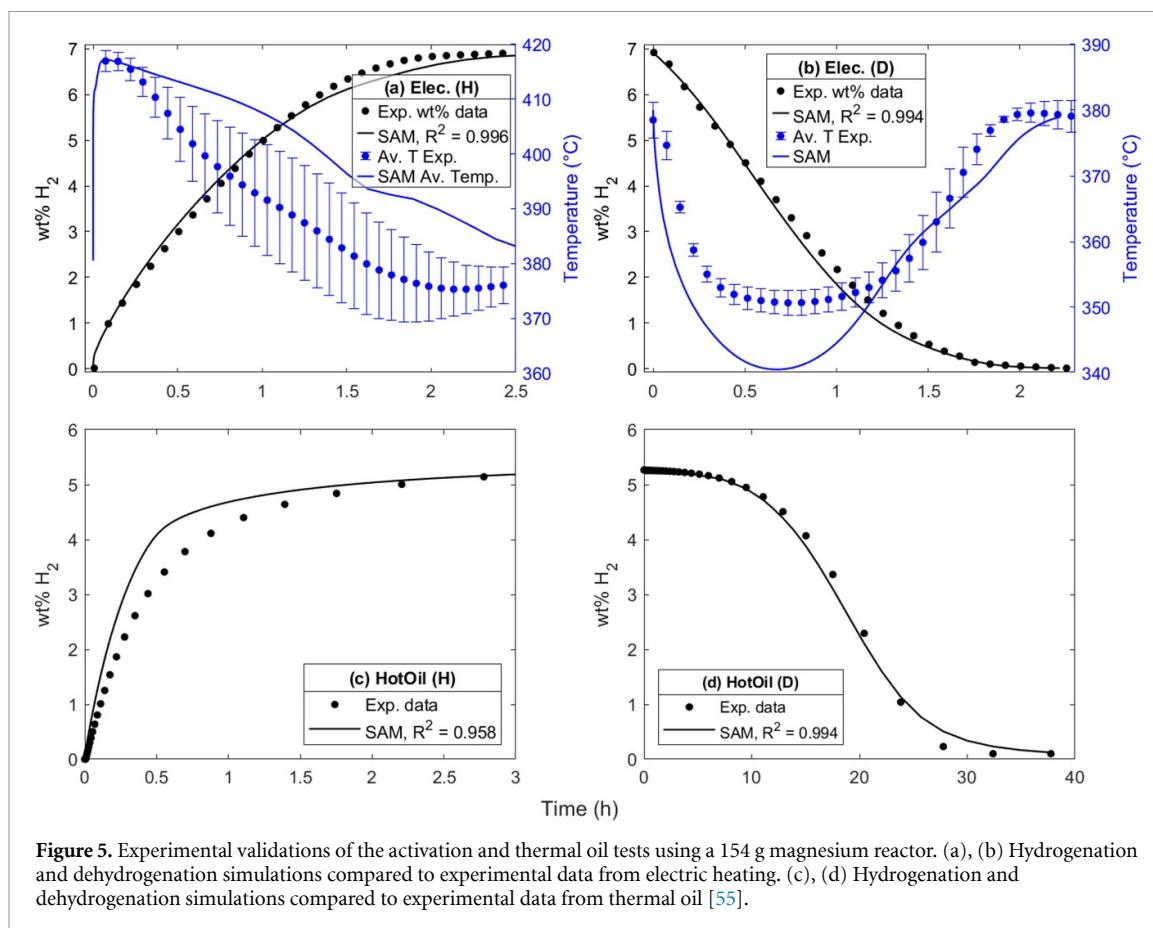
**Figure 5.** Experimental validations of the activation and thermal oil tests using a 154 g magnesium reactor. (a), (b) Hydrogenation and dehydrogenation simulations compared to experimental data from electric heating. (c), (d) Hydrogenation and dehydrogenation simulations compared to experimental data from thermal oil [55].

Reaction + Fragmentation) dehydrogenation of magnesium hydride uses rate equation (7), with the desorption site availability as $\sigma_{\mathrm{D}} = (P_{\mathrm{B}} - P_{\mathrm{g}})/P_{\mathrm{B}}$, and $P_{\mathrm{B}}$ represented by equation (11).

Twenty five cycles were performed for activation using electric heating. The concentration profiles from run 006 to 025 were similar and used a pressure of 25 bar controlled by a regulator. A typical activation run is shown in figures 5(a) and (b). From figures 5(a) and (b) the concentration profile show good fits ($R^2 > 0.99$). Considering the temperature profiles, the trajectories are similar but show deviation; this is attributed to the differences in experimental setup compared to the thermal physics assumptions used within the model. The first reason was because an adiabatic boundary condition was assumed at the top and bottom of reactor domain, where there was poor insulation at the reactor ends. The second reason was assuming a constant temperature boundary condition for the heating element. In reality, a heating tape was used that did not achieve a constant temperature through the entire length of tape, due to a change in power demand (from the PID controller) and non-uniform resistance heating along the length of the tape. The third reason was approximating the copper helical spiral as a group of tori.

For the hot oil scenarios, the magnesium required re-activation due to repetitive temperature ramping required to commission the hot oil circuit and shut down periods due to Covid-19 lockdown lab closures. Due to the hot oil circuit being limited at 300 °C, only partial re-activation was achieved (5 wt% instead of 7 wt% during activation), where this meant heat transfer to the oil was insufficient. 14 runs in total were undertaken using thermal oil. For hydrogenation, the operating conditions were 302 °C and 9–14 bar(g) and for dehydrogenation, 302 °C and −0.65 bar(g), with an oil flow rate of 6 nl min$^{-1}$. The results of a typical run are shown in figures 5(c) and (d). Despite the issues as per above, it is clear the SAM displays robustness and has modelled the hot oil experimental data for hydrogenation and dehydrogenation with reasonable accuracy.

In effect, the results in figure 5 of a 154 g magnesium test store demonstrate the potential feasibility of the SAM (all fits display $R^2 > 0.95$). This indicates prospective scalable characteristics when using the SAM for modelling magnesium hydride TCES systems.

## 2.2. Recent development of multiscale modelling capabilities of relevant MHs for thermal storage
### 2.2.1. Mesoscale modelling of microstructure-aware thermal conductivity of MHs
As the TES mechanism of MHs relies on utilising the enthalpy of reaction, if the reaction rate is limited by poorly controlled heat transport and dissipation during hydrogenation/dehydrogenation cycles, then this
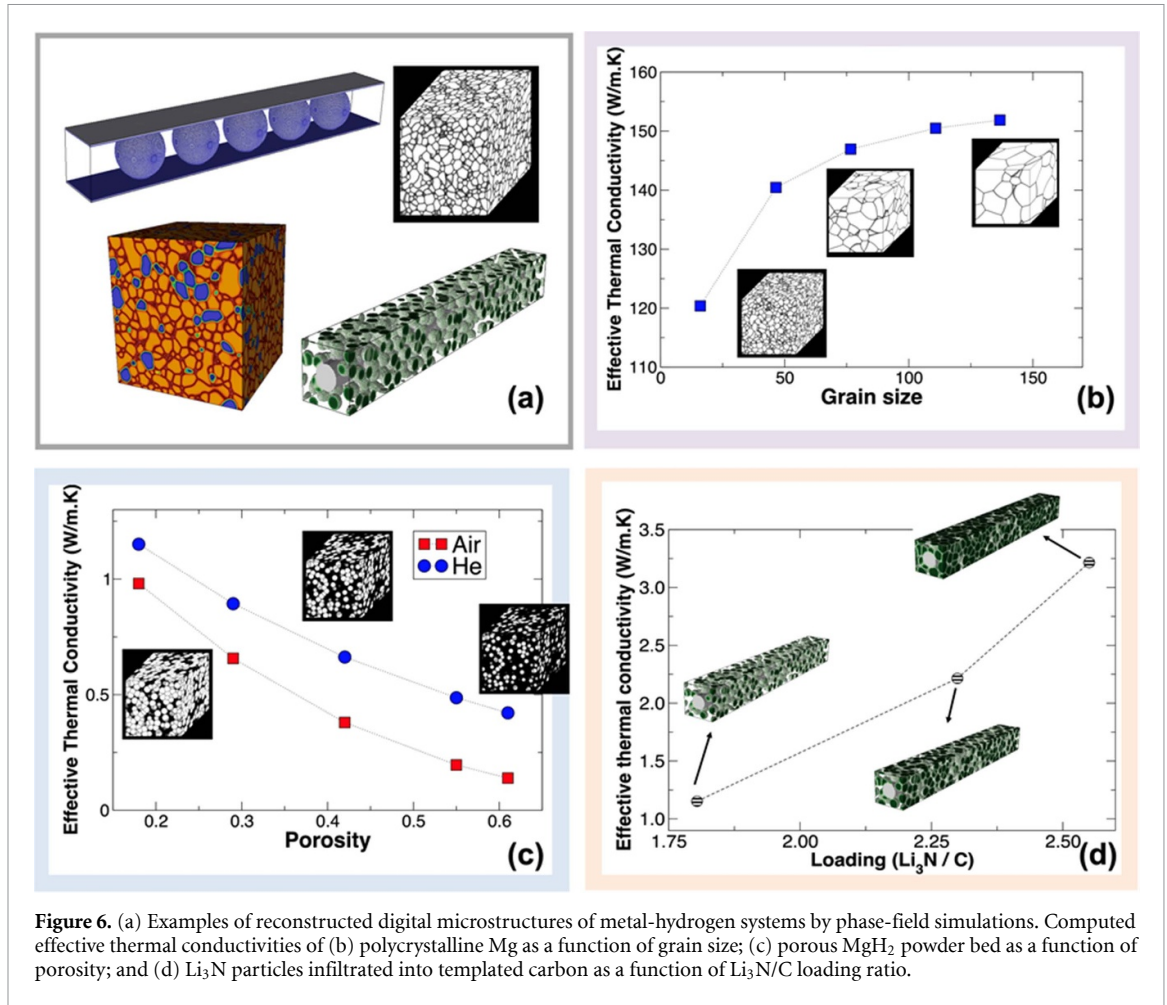
**Figure 6.** (a) Examples of reconstructed digital microstructures of metal-hydrogen systems by phase-field simulations. Computed effective thermal conductivities of (b) polycrystalline Mg as a function of grain size; (c) porous $MgH_2$ powder bed as a function of porosity; and (d) $Li_3N$ particles infiltrated into templated carbon as a function of $Li_3N/C$ loading ratio.

will result in limited TES performance. Thermal transport properties of materials are known to depend on several microstructural features, including particle/grain size, morphology, connectivity, packing density (or porosity), and so forth. Therefore, achieving efficient thermal management by tailoring microstructures of metal-hydrogen systems is one of the viable engineering strategies for improving the TES performance of MHs. To this end, the mesoscopic modelling framework provides a useful computational tool for systematically investigating the relationship between complex microstructure and thermal transport property of MHs. LLNL has established and validated an efficient mesoscale modelling framework for computing effective thermal conductivities of realistic microstructures [57]. This approach combines two mesoscale modelling methods: (a) a digital microstructure generator to reconstruct experimentally relevant microstructures of materials; and (b) an efficient numerical approach to solve the steady-state thermal conduction equation. Within the modelling framework, the digital representations of associated microstructures of TES materials are first generated. Some examples from mesoscale simulations based on the phase-field approach [58, 59] are shown in figure 6(a). Based on the experimental information, a variety of microstructures can be emulated, including single phase polygranular structure, mixtures of multiple materials, and particles encapsulated by host materials, as shown in the figure. We then assign thermal conductivities to individual grains, materials, gases, and/or interfaces, resulting in site-specific thermal conductivity in the microstructure. To extract the ETC, the steady-state temperature profile within the microstructure is obtained by numerically solving the following steady-state thermal conduction equation,

$$\nabla_i \cdot \left[ \lambda_{ij} \left( \overrightarrow{r} \right) \nabla_j T \left( \overrightarrow{r} \right) \right] = 0 \tag{19}$$

where $\lambda_{ij}(\vec{r})$ represents the site-specific (or position-dependent) thermal conductivity and $T$ is the local temperature, using the Fourier-spectral iterative perturbation method. The established method has been applied to diverse types of microstructures of metal, composite, or metal-hydrogen systems, which can be utilized for hydrogen/TES. Figures 6(b)–(d) include three examples: (a) polycrystalline Mg with different grain sizes (figure 6(b)); (b) $MgH_2$ powder bed (spherical particles) with different porosity (figure 6(c)); and (c) $Li_3N$ particles infiltrated into templated carbon with different $Li_3N/C$ loading ratio (figure 6(d)). Note

that we use the interpolation of conductivities of adjoining grains or phases for defining the interfacial conductivity for $\lambda_{ij}(\vec{r})$ in these examples due to the lack of information about interfacial properties for the given materials systems. However, we emphasize that the site-specific conductivity model is mathematically general, allowing for incorporation of specific interfacial thermal conductivities once determined.

As shown in our modelling results in figures 6(b)–(d), our methodology clearly captures the impacts of microstructural features, including grain sizes, porosity, and loading ratio for example, on the ETC. Notably, this analysis could inform future materials-driven modifications to system-level TES models. Instead of using fixed parameters in the system-level engineering models, the materials parameters (e.g. thermal conductivity) can vary as a function of microstructural features and reaction progress in the engineering models, leading to more realistic TES performance prediction. It is worth pointing out key aspects within the modelling framework, which need to be further improved for more quantitative prediction. First, the interfacial thermal conductivities need be better parameterized based on well-defined measurements and/or computations. As we discussed above, the current model assumes the interfacial conductivity as the interpolation of conductivities of adjoining materials. This can be replaced by the more accurate interfacial conductivity once it is known. Second, the input digital representations of microstructures can be more realistic to account for complex features of the experimental microstructures. This requires more detailed experimental characterizations of the storage material microstructures (e.g. phase fraction, particle size distribution, particle morphology, porosity, etc) at different stages of the reaction, which may allow for reconstruction of digital microstructures that are equivalent to experimental ones. Third, more sampled cases of microstructural configurations should be considered for statistically reliable prediction. For the given microstructural condition (e.g. grain size, porosity, phase fraction, etc), there exist various different configurations of microstructural features such as particles, grains, and phases within a material. Accordingly, we can consider corresponding several digital microstructures for the ETC calculations, providing the variability of the predicted conductivity values for the given microstructural condition. This would be important for quantifying the uncertainty of the prediction.

*2.2.2. Integrated multiscale model for full simulation of (de)hydrogenation of MHs*
The efficiency of TES mechanisms is determined by the (de/re)hydrogenation kinetics of MHs during operation. Predicting the (de/re)hydrogenation kinetics of MHs incorporating complex microstructures is not straightforward due to concurrent and coupled multiple chemical, physical, and materials processes. To systematically investigate the associated kinetic behavior, LLNL has developed an integrated multiscale model that comprehensively couples the temperature-sensitive processes, including chemical reaction, diffusion, stress, and phase transformations, which occur at multiple length- and time scales. The model is based on the mesoscale phase-field method for simulating hydride microstructure evolution in polycrystalline materials [60]. This model allows us to simulate full (de)hydrogenation reactions of metal-hydrogen systems incorporating realistic microstructures. By analysing the simulated kinetic (de)hydrogenation and associated microstructure evolution, we can explore which specific materials parameters could have the highest impact on overall kinetics. Figure 7(a) shows examples of simulated hydrogenation of model polygranular metal-hydrogen systems with three different grain sizes. We can monitor the temporal evolution of hydrogen content and the associated hydride microstructure within the storage medium (see figure 7(a)), as well as the coevolving latent heat of reaction (see figure 7(b)). Although further refinement and calibration are underway, this example demonstrates the utility of this model. This model is now being extended to account for realistic parameters for the promising MHs for TES, as well as to quantify the thermal efficiency by implementing more refined microstructure-level models for local latent heat release/absorption and thermal transport within the modelling framework. We also caution here that the model incorporates some challenges, which need to be overcome for more quantitative modelling and simulations. Since this model couples several temperature-sensitive chemical, physical and material processes, it involves a variety of input model parameters. Although many of these parameters can be obtained from atomistic calculations and/or experimental measurements, some parameters cannot be easily estimated (e.g. pre-factors for chemical reactions, interface migration mobility, etc). These parameters need to be determined by calibrating simulated and measured (de)hydriding kinetics or latent heat evolution under controlled conditions.

## 3. Practical thermal stores—materials and challenges

### 3.1. Tuning the thermodynamics of MHs for high temperature thermochemical energy storage (TCES)
The thermodynamics of MHs dictate the operating conditions when utilised as a TCES material, for example, if we consider $CaH_2$,
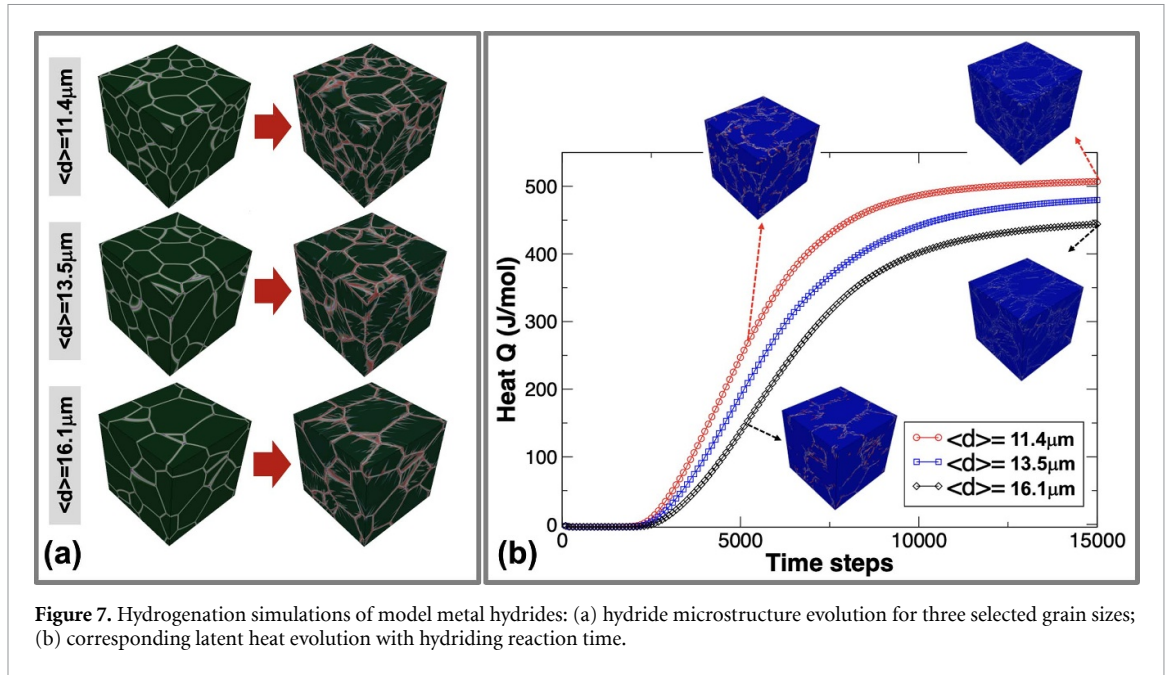
**Figure 7.** Hydrogenation simulations of model metal hydrides: (a) hydride microstructure evolution for three selected grain sizes; (b) corresponding latent heat evolution with hydriding reaction time.
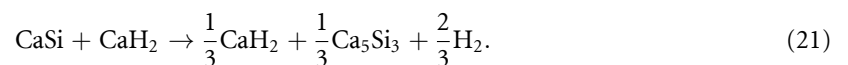
$$CaH_{2(s)} \rightleftharpoons Ca_{(s)} + H_{2(g)} \tag{20}$$

where the $\Delta H = 207.9 \text{ kJ mol}^{-1}$ H$_2$ and $T_{dec}(1 \text{ bar}) \approx 1000\,°C$. The operating temperature and pressure inherently affect each other via the van't Hoff equation [15, 61], see equation (11).

While many MHs release hydrogen at elevated temperatures, few have shown reliable cyclic hydrogen capacity, which is a requirement if the material is to be utilised in applications. Others would be hindered in application by excessive cost even if cyclic efficiency were to be achieved. At temperatures above 250 °C it is rare for MHs to consistently cycle hydrogen without the requirement of an additive to prevent sintering and agglomeration. Certain MHs suffer from other issues such as an operating temperature that is too high for commercial application such as CaH$_2$ shown above, equation (20); or has a too low an operational temperature with resultant lower efficiency electricity generation, such as MgH$_2$ that decomposes under 1 bar of hydrogen pressure at a temperature of $T_{dec}$ (1 bar) = 274 °C [62]. While 400 °C would result in a manageable operating pressure of 20–25 bar H$_2$, operation of MgH$_2$ at a higher temperature would raise the pressure too high ($\approx$110 bar H$_2$ at 500 °C) [63]. To modify the inherent operating temperature limitations of MHs and enable them as efficient TES materials, studies have been carried out to thermodynamically destabilise (or stabilise) MHs to tune the temperature, at which hydrogen can be cycled, into a practical operating window.

CaH$_2$ has been identified as a potential TES material as it has a practical energy density of 4198 kJ kg$^{-1}$ and low cost of 2.6 € kWh$_{th}^{-1}$ [15]. However, decreasing the operating conditions to between 600 °C and 800 °C with an operating hydrogen pressure of 1–10 bar is required to make it practical for next generation energy storage systems. Several studies have recently been carried out to achieve these operating conditions using cost effective materials as thermodynamically destabilising additives.

For example, Griffond *et al* studied CaH$_2$ with the addition of varying molar ratios of Si [64]. Through initial theoretical investigations, the optimal ratio of 2:1 CaH$_2$:Si was determined and this system was studied to determine the decomposition pathway and thermodynamic properties. The decomposition pathway is a multi-step process, but the reaction of interest is shown in equation (22). The operating temperature was determined to be 747 $\pm$ 33 °C at 1 bar H$_2$ pressure with $\Delta H_{des} = 154 \pm 4 \text{ kJ mol}^{-1}$ H$_2$ and $\Delta S_{des} = 151 \pm 3 \text{ J mol}^{-1} \text{ K}^{-1}$ H$_2$.

$$CaSi + CaH_2 \rightarrow \frac{1}{3}CaH_2 + \frac{1}{3}Ca_5Si_3 + \frac{2}{3}H_2. \tag{21}$$

Sofianos *et al* achieved destabilisation of CaH$_2$ using the halides of calcium (CaCl$_2$, CaBr$_2$, and CaI$_2$) to form their binary compounds (CaHCl, CaHBr, and CaHI, respectively), where hydrogen desorption was observed between 700 °C and 800 °C with working pressures of 1–10 bar H$_2$ [65]. The samples were synthesised by milling and annealing of the MH and respective halide under a H$_2$ atmosphere before determining the physical properties of the material. Decomposition of the calcium hydride-halides resulted in the formation

of the calcium halide along with pristine calcium metal. Segregation, melting, and sintering caused extremely slow reabsorption kinetics of hydrogen and thus resulted in new obstacles for these particular systems.

Balakrishnan *et al* used Zn metal to facilitate the thermodynamic destabilisation of $CaH_2$ [66]. When Zn was milled in a 1:3 ratio with $CaH_2$ the decomposition temperature of the mixture was measured to be 597 °C at 1 bar $H_2$ pressure. The reaction pathway of the $CaH_2$–Zn mixture was a three-step process following the formation of $CaZn_{13}$, $CaZn_{11}$, and finally $CaZn_5$. The material was shown to reversibly cycle with the formation of $CaH_2$ according to reaction (22). Ten hydrogenation cycles were carried out at 580 °C, where a reduction of 20% capacity was observed. This capacity loss was attributed to the evaporation of Zn from the alloys. The enthalpy and entropy of formation of reaction (23) was found to be $\Delta H_{des} = 131 \pm 4$ kJ mol$^{-1}$ $H_2$, $\Delta S_{des} = 151 \pm 4$ J mol$^{-1}$ K$^{-1}$ $H_2$ respectively, providing a $T_{dec}$ (1 bar) = 597 $\pm$ 35 °C.

$$CaH_2 + \frac{5}{6}CaZn_{11} \rightleftharpoons \frac{11}{6}CaZn_5 + H_2. \tag{22}$$
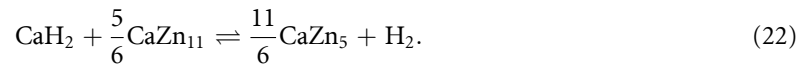
Alumina is also an efficient additive for the thermodynamic destabilisation of $CaH_2$ [67]. When mixed in a 2:1 ratio ($CaH_2$:$Al_2O_3$) multiple reversible hydrogen cycles are achieved, with the formation of $Ca_{12}Al_{14}O_{33}$. Thermodynamic measurements using Sieverts' apparatus determined a $\Delta H_{des} = 100 \pm 2$ kJ mol$^{-1}$ $H_2$ and $\Delta S_{des} = 110 \pm 2$ J mol$^{-1}$ K$^{-1}$ $H_2$, providing a $T_{dec}$ (1 bar) = 636 °C for reaction (24).

$$3CaH_2 + 2Al_2O_3 \rightleftharpoons \frac{1}{7}Ca_{12}Al_{14}O_{33} + \frac{9}{7}CaO + 2Al + 3H_{2(g)}. \tag{23}$$
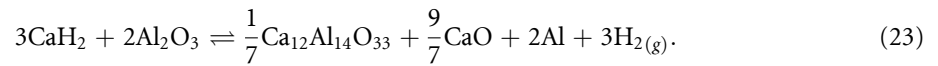
In comparison, $Al_2O_3$ has been investigated in connection with other TES materials, for example metal carbonates with promising results [24]. A $CaCO_3$–$Al_2O_3$ system was shown to form a $Ca_5Al_6O_{14}$ compound, which in contrast to the formed mayenite, $Ca_{12}Al_{14}O_{33}$, in the $CaH_2$–$Al_2O_3$ system [67], does not take part in the reverse reaction but rather acts as a catalyst enabling a 90% energy capacity retention over 500 $CO_2$ cycles [24]. Thus, ternary aluminium-containing compounds seem to have a positive effect on TES materials and may be worth further investigation in connection with MHs.

Strontium hydride has an energy density of 2041 kJ kg$^{-1}$ and would be a more promising TES material if its high operating temperature, $T_{dec}$ (1 bar) of $\approx$ 1070 °C, was decreased [68]. Humphries *et al* have used aluminium to thermodynamically destabilise $SrH_2$ by mixing them in a 1:4 ratio [69]. This system was expected to proceed similar to the $CaH_2$ + 4Al system that was shown to reversibly cycle $H_2$ at 600 °C under $\approx$ 3 bar $H_2$ pressure [70]. As expected, the thermal decomposition of the $SrH_2$ + 4Al follows a two-step process with the final formation of $SrAl_2$. The material was demonstrated to cycle 50 times at 867 °C by varying the $H_2$ pressure between 0.5 and 3 bar following equation (25), although a reduction in cycling capacity was observed. The measured thermodynamics of $\Delta H_{des} = 132 \pm 2$ kJ mol$^{-1}$ $H_2$ and $\Delta S_{des} = 118 \pm 2$ J K$^{-1}$ mol$^{-1}$ $H_2$ result in a $T_{dec}$(1 bar) of 846 °C.

$$\frac{1}{2}SrH_2 + \frac{1}{2}SrAl_4 \rightleftharpoons SrAl_2 + \frac{1}{2}H_2. \tag{24}$$
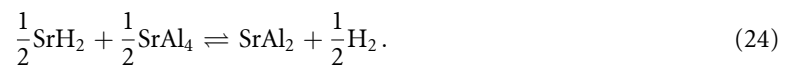
Similar manipulation of thermodynamics are reported for high-temperature metal carbonates, i.e. $Li_2CO_3$ and $BaCO_3$ ($T_{dec}$ > 1200 °C) where the decomposition reaction is altered through the formation of a metal orthosilicate, $M_xSiO_4$ [25, 71], to release $CO_2$ gas at lower temperature (>650 °C), e.g.

$$BaCO_3 + BaSiO_3 \rightleftharpoons Ba_2SiO_4 + CO_{2(g)}. \tag{25}$$
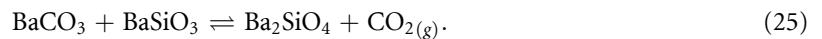
Hence, the gas release temperature is significantly reduced. The above examples (equations (21) through (25)) highlight the potential of chemically manipulating materials to rationally design systems to desired operating conditions.

Thermodynamic stabilisation (rather than destabilisation) of materials has also been explored to increase the operating temperature of materials. Previous studies have shown that fluorine substitution into MHs such as NaH, $MgH_2$, and $NaMgH_3$ is a tuneable and cost-effective method of achieving optimal characteristics for TES materials with an increase in operating temperature [62, 72–74]. The fluorine addition also causes an associated reduction in evaporation of the base metals, which can have an inherently high vapour pressure, thus making the solid-state compound more stable over time at high temperature. Studies have been carried out on the $NaH_xF_{1-x}$ and $Mg(H_xF_{1-x})_2$ ($x$ = 1, 0.95, 0.85, 0.7, 0.5, 0) systems to further the understanding of these solid-solutions [75, 76]. $NaH_xF_{1-x}$ materials were studied by synchrotron radiation x-ray and nuclear magnetic resonance (NMR) spectroscopy, which determined that yielding a single phase solid-solution is difficult even after annealing precursor fluorides and hydrides under $H_2$
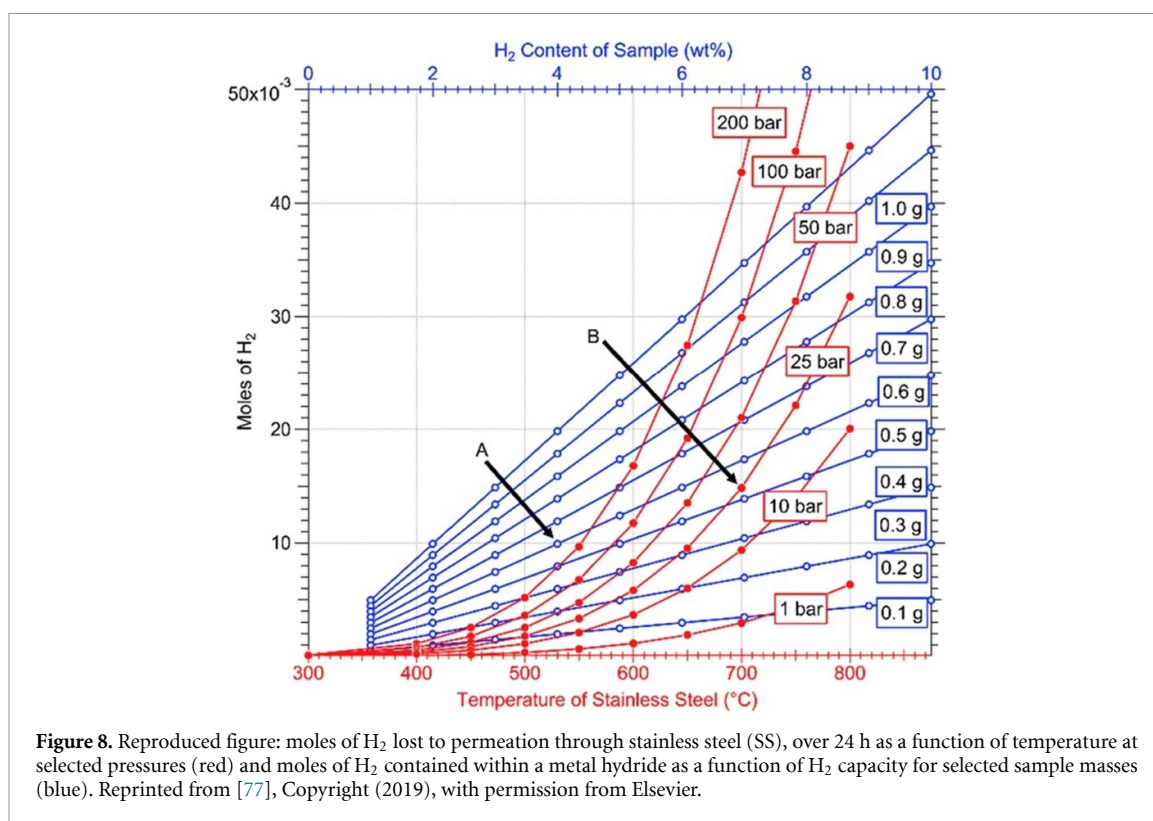
**Figure 8.** Reproduced figure: moles of $H_2$ lost to permeation through stainless steel (SS), over 24 h as a function of temperature at selected pressures (red) and moles of $H_2$ contained within a metal hydride as a function of $H_2$ capacity for selected sample masses (blue). Reprinted from [77], Copyright (2019), with permission from Elsevier.

pressure for six days at 450 °C [75]. Not only does fluorine substitution increase the thermal stability of NaH but it also increases the melting point of the material. As such $NaH_{0.85}F_{0.15}$ melts above 750 °C whereas pure NaH melts at 625 °C (both under a $H_2$ atmosphere). This means that these materials may be useful as phase change TES materials. Inelastic neutron spectroscopy, corroborated by DFT studies, was carried out on the $Mg(H_xF_{1-x})_2$ system as to determine the structural dynamics between the solid solutions and pure components [76]. A significant upshift in frequencies of optical phonon was observed and reflects the enhancement of ionicity in $Mg(H_xF_{1-x})_2$ with increasing fluoride content, as $F^-$ is of larger electronegativity to hydrogen, which consequently draws more electrons from Mg compared to $H^-$.

### 3.2. Challenges of measurements of thermodynamics of MHs in high temperature stores

Accurately determining the physical properties of MH's allows for the optimisation of the operating conditions of a TES plant and also allows for more accurate estimation of capital and running costs. Hydrogen is known to have a high solubility and permeability in stainless steel (SS) at elevated temperature (significant above 500 °C). As such, hydrogen can diffuse through the walls of a heated SS vessel. Figure 8 illustrates this. For example, an MH sample of 0.5 g with four $H_2$ wt% would uptake 10 mmol of $H_2$ (point A), whereas the permeation over a 24 h period through the sample cell at 700 °C and 25 bar would be 15 mmol of $H_2$ (point B). This is based on a sample cell of 8 cm tube length and 0.21 cm wall thickness [77].

This makes accurate determination of thermodynamics, kinetics of hydrogen absorption/desorption, thermodynamic plateau shape, and practical hydrogen content difficult, especially if the reaction kinetics are poor or temperatures are high. Experimental measurements have previously used quartz, silica, heavy walled SS, or double walled SS sample cells, but each of these have their disadvantages [77]. Quartz and silica reactors can only operate at low pressure, while the advanced stainless-steel reactors suffer from hydrogen solubility, can be expensive to construct, and hence experiments become more complex. New hydrogen resistant materials for reactors have been studied to find an optimal material that can operate at high temperatures and pressures, is easy and cheap to construct, and does not suffer from hydrogen embrittlement, permeability, or solubility. A number of options have been considered including different metals, ceramics, and coatings. It was deemed that SS coated with $Al_2O_3$ is acceptable although coating the parts can be difficult and inhomogeneous [77]. In addition, the reactors must be handled carefully to avoid damage of the coating, which would lead to permeation of $H_2$ through the defect. If an SS reactor (coated or uncoated) is to be used then a coefficient may be calculated and applied to calculations to account for the hydrogen loss through the vessel walls [77]. SiC vessels offer high hydrogen permeation resistance at high temperatures, reasonable pressure ratings (due to their high tensile strength [78]), and are commercially available, however, at prices considered high for large-scale applications.
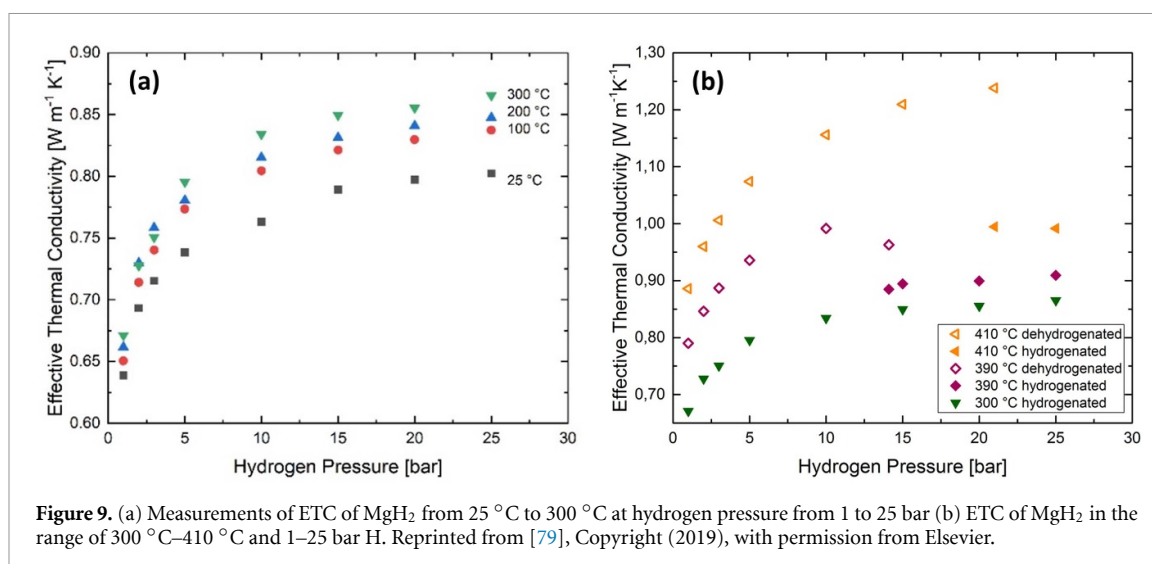
**Figure 9.** (a) Measurements of ETC of MgH$_2$ from 25 °C to 300 °C at hydrogen pressure from 1 to 25 bar (b) ETC of MgH$_2$ in the range of 300 °C–410 °C and 1–25 bar H. Reprinted from [79], Copyright (2019), with permission from Elsevier.
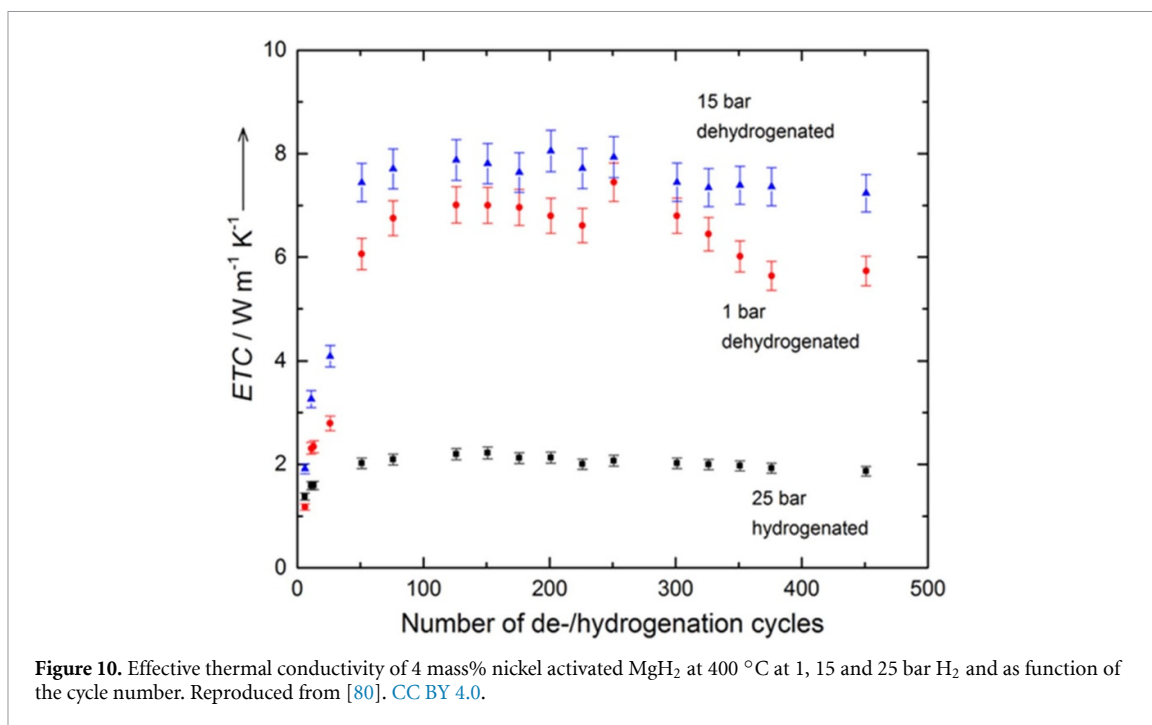
### 3.3. Challenges of thermal conductivity measurements

The thermal transport properties of a TES material are also important to understand as they are essential in determining the heat flow through a powder bed. The thermal conductivity of a material affects how fast heat can be dissipated from the different regions of the reactor into the heat extraction system (and vice versa) and may ultimately induce local differences in reaction kinetics or pathways. A major drawback of MH packed beds for heat storage applications is the low heat conductivity of the storage material. If the ETC of the powder bed is poor then the reactor can be designed to optimise heat transport, e.g. by internal heat fins, addition of thermally conductive additives to the powder, or decreasing the maximum distance between the heat transfer system and the powder. Measuring the specific heat of a material is useful when calculating the characteristics of the reactor as although these materials produce heat through thermochemical reactions, they also have a sensible heat contribution to the energy storage/release. Due to the air sensitive nature of MHs, measurement of their thermal properties can be difficult unless conducting the experiments under an inert (or H$_2$) atmosphere, while the measurements are also highly dependent on the density and preparation of the powder. Thus, the thermal transport properties have only been determined for a small selection of MHs, which, unfortunately, are not directly comparable due to different preparation techniques and varying experimental conditions.

The ETC or $\lambda_e$ is not a specific property of the material, it is the combination of a variety of single transport mechanisms as conduction, convection, and radiation [79]. In addition, densification, inhomogeneity, scale up and purity of the material need to be considered to optimize the system heat transfer. ETC values of the Mg/MgH$_2$ system under operating conditions up to 25 bar hydrogen pressure and temperatures up 410 °C were recently reported [79]. The Transient Plane Source method was used to measure the thermal conductivity of the MH under varying hydrogen pressures at given temperatures. Measurements of effective thermal conductivity in fully hydrogenated MgH$_2$ were performed in the temperature range from room temperature up to 300 °C and between 1 and 25 bar of hydrogen pressure. The ETC values depend on the hydrogen pressure, especially in the region of up to 15 bar. The ETC values for all presented temperatures achieve 0.65 W m$^{-1}$ K$^{-1}$ at ambient pressure and increase to 0.80–0.85 W m$^{-1}$ K$^{-1}$ at 25 bar in the temperature range between 25 °C and 300 °C (figure 9(a)).

Figure 9(b) shows the results of ETC measurements of hydrogenated and dehydrogenated MgH$_2$. It was shown that the ETC at 410 °C and 25 bar hydrogen pressure increases by 10% from 1.0 W m$^{-1}$ K$^{-1}$ to 1.1 W m$^{-1}$ K$^{-1}$ after 18 discharging and charging cycles for hydrogenated MgH$_2$. For dehydrogenated MgH$_2$ this increase in ETC was much higher at 50% from 1.20 W m$^{-1}$ K$^{-1}$ to 1.80 W m$^{-1}$ K$^{-1}$ and at 21 bar hydrogen pressure [80].

The effective thermal conductivity of the magnesium hydride powder bed changes with the number of de-/hydrogenation cycles. This is due to the expansion of the magnesium particles by about 30% during the hydrogenation and the potential to sinter in the dehydrogenation phase at the higher temperatures. Recently, the thermal conductivity measurements of Ni-doped MgH$_2$ (4 mass% Ni powder) over more than 500 cycles was published, figure 10. It could be shown that a long-term cycling process has a significant influence on the ETC [80]. The measurements were carried out at 400 °C and at hydrogen pressures of 1, 15 and 25 bar. During the first 100 cycles, an increase in the ETC value was observed. At 1 bar H$_2$ (dehydrogenated state), the ETC value increased from an initial value of 1.17 Wm$^{-1}$ K$^{-1}$– 6.75 W m$^{-1}$ K$^{-1}$ after 76 cycles and

**Figure 10.** Effective thermal conductivity of 4 mass% nickel activated $MgH_2$ at 400 °C at 1, 15 and 25 bar $H_2$ and as function of the cycle number. Reproduced from [80]. CC BY 4.0.

reached a maximum value of 7.45 W m$^{-1}$ K$^{-1}$ after 251 cycles. At 15 bar $H_2$ pressure, a slightly higher value of 8.05 W m$^{-1}$ K$^{-1}$ was observed. A similar observation with increasing ETC value was also found for the hydrogenated material (25 bar $H_2$ pressure). The overall increase is lower, but a maximum value of 2.22 W m$^{-1}$ K$^{-1}$ is reached after 151 cycles.

Bird *et al* have recently measured the effective thermal conductivity (ETC), thermal diffusivity, and heat capacity of 10 MH's under identical conditions [81]. Each of the samples (13 mm pellets compressed at 370 MPa) were measured under an argon atmosphere at room temperature. This allows for the direct comparison of the thermal transport properties of materials and also provides valuable information for reactor design and numerical modelling studies. Carbonates and metal oxides are, besides MHs, prominent representatives of TCES materials and have been included in the investigations. Thermal diffusivity describes the rate of heat transfer of a material from the hot to the cold side. It can be calculated from the thermal conductivity divided by the product of density and the specific heat capacity and is a specific constant for each material. As shown in table 1, the ETC of LiH and NaF are higher than the other listed materials, 11.0 W m$^{-1}$ K$^{-1}$ and 9.4 W m$^{-1}$ K$^{-1}$, respectively. By adding different amounts of graphite or exfoliated natural graphite ENG, it can be shown that the thermal properties can be modified. For $Mg_2FeH_6$ without any additives, an ETC of 1.80 W m$^{-1}$ K$^{-1}$ could be determined. When 5 wt% ENG was added, the ETC increased to 4.43 W m$^{-1}$ K$^{-1}$ and to 6.76 W m$^{-1}$ K$^{-1}$ with an amount of 10 wt% ENG.

### 3.4. Challenges of reactor design

#### 3.4.1. General reactor design and orientation

Along with material design and characterisation challenges, there are also reactor design issues to overcome. In general, three established reactor types have been tested for hydride based TCES. These are shell and tube, internal/external helical flow and double pipe reactors, and their variations. Double pipe, although the simplest to design will enable the lowest HTF flow rate of three, followed by helical flow and then shell and tube [82]. In section 4, a novel large scale pillow plate reactor and its development is detailed.

There are several considerations of reactor choice on scale-up. Every cycle involves hydrogen pressure swing at temperatures >400 °C, where a reactor with 25+ year time will require $\approx$ 10 000 daily cycles. Mechanical design must be considered here, and the most robust, cost-effective choice would be powder in a tube, as a thicker tube can be specified. From a mechanical perspective, an external helical flow jacket is suitable, but an internal helical flow (without a central strengthening tube) although advantageous from a heat management viewpoint may be problematic for long reactor lengths and require a central strengthening tube with resultant lower powder capacity.

Considering a double pipe reactor, a larger radius is desirable due to the ability to pack in more powder. However, this increase in radius causes a rise in powdered bed thermal resistance, which is detrimental to the reaction rate of the MH store. Methods to reduce the thermal resistance are common, such as using fins or

**Table 1.** Effective thermal conductivity ($\lambda_e$), thermal diffusivity ($\kappa$), heat capacity per volume ($C$) and crystallographic densities ($\rho$) of selected materials using the transient plane (TPS) method. Standard deviations are in parentheses. Reproduced from [81] with permission from the Royal Society of Chemistry.
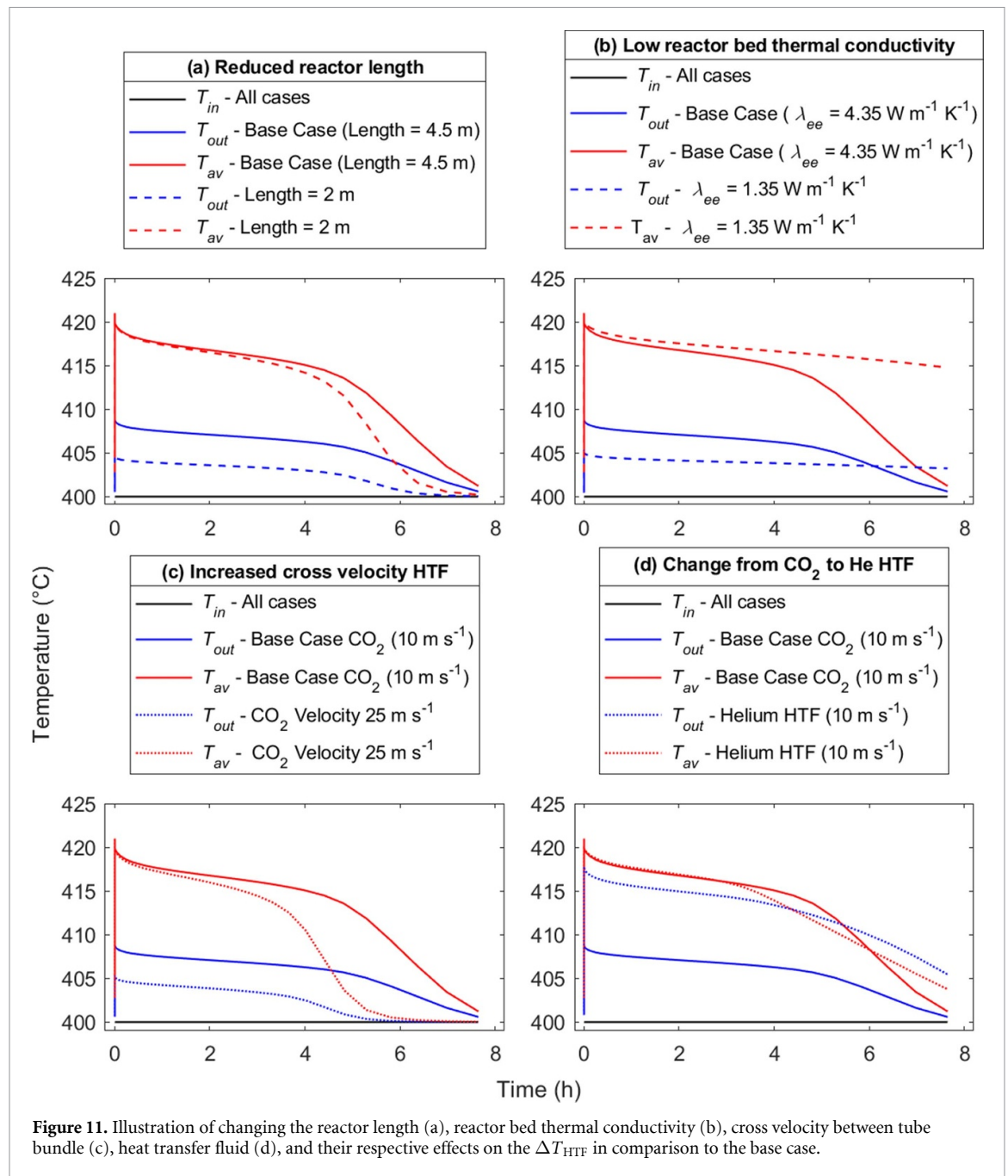
| Material | $\lambda_e$ (W m$^{-1}$ K$^{-1}$) | $\kappa$ (mm$^2$ s$^{-1}$) | $C$ (MJ m$^{-3}$ K$^{-1}$) | (g cm$^{-3}$) |
|---|---|---|---|---|
| CaH$_2$ | 3.10 ($\pm$0.07) | 1.8 ($\pm$0.1) | 1.7 ($\pm$0.2) | 1.90 |
| CaO | 0.83 ($\pm$0.01) | 0.4 ($\pm$0.02) | 2.10 ($\pm$0.09) | 3.34 |
| K$_2$CO$_3$ | 0.55 ($\pm$0.01) | 0.37 ($\pm$0.02) | 1.50 ($\pm$0.07) | 2.29 |
| KBH$_4$ | 1.03 ($\pm$0.01) | 0.70 ($\pm$0.01) | 1.50 ($\pm$0.03) | 1.11 |
| LiAlH$_4$ | 1.30 ($\pm$0.01) | 0.66 ($\pm$0.04) | 1.9 ($\pm$0.1) | 0.917 |
| LiBH$_4$ | 1.30 ($\pm$0.01) | 0.54 ($\pm$0.05) | 2.4 ($\pm$0.2) | 0.67 |
| LiH | 11.0 ($\pm$0.3) | 1.1 ($\pm$0.2) | 9.0 ($\pm$0.1) | 0.78 |
| 2 Mg + Fe | 2.20 ($\pm$0.04) | 1.8 ($\pm$0.1) | 1.2 ($\pm$0.08) | 2.98 |
| Mg$_2$FeH$_6$ | 1.80 ($\pm$0.02) | 1.29 ($\pm$0.07) | 1.39 ($\pm$0.07) | 2.74 |
| Mg$_2$FeH$_6$ + 10 wt% Fe | 1.72 ($\pm$0.03) | 1.4 ($\pm$0.1) | 1.3 ($\pm$0.1) | — |
| Mg$_2$FeH$_6$ + 25 wt% Fe | 1.73 ($\pm$0.03) | 1.45 ($\pm$0.08) | 1.20 ($\pm$0.08) | — |
| Mg$_2$FeH$_6$ + 5 wt% ENG | 4.43 ($\pm$0.05) | 2.57 ($\pm$0.08) | 1.73 ($\pm$0.07) | — |
| Mg$_2$FeH$_6$ + 10 wt% ENG | 6.76 ($\pm$0.03) | 1.8 ($\pm$0.2) | 3.7 ($\pm$0.3) | — |
| Na$_2$CO$_3$ | 0.56 ($\pm$0.01) | 0.36 ($\pm$0.02) | 1.60 ($\pm$0.08) | 2.54 |
| NaAlH$_4$ | 1.90 ($\pm$0.02) | 0.88 ($\pm$0.06) | 2.2 ($\pm$0.2) | 1.24 |
| NaBH$_4$ | 0.97 ($\pm$0.01) | 0.4 ($\pm$0.03) | 2.4 ($\pm$0.1) | 1.07 |
| NaF | 9.4 ($\pm$0.1) | 1.8 ($\pm$0.2) | 5.5 ($\pm$0.6) | 2.78 |
| NaH | 5.00 ($\pm$0.07) | 1.1 ($\pm$0.1) | 4.7 ($\pm$0.4) | 1.39 |
| NaMgH$_3$ | 1.90 ($\pm$0.02) | 3.2 ($\pm$0.2) | 0.58 ($\pm$0.04) | 1.47 |
| NaMgH$_3$ + 20 wt% ENG | 5.15 ($\pm$0.07) | 2.16 ($\pm$0.14) | 2.4 ($\pm$0.2) | — |

compacts. For example, adding graphite to a hydride and compression into a compacts yields a $\lambda_e$ in the range of 5–8 W m$^{-1}$ K$^{-1}$ [83–85] and as shown in table 1. The other advantage of compacts is the increase in bulk density. Maximising the bulk density will significantly save costs as the number of reactors required is reduced [37, 55].

Without the addition of fins or other heat transfer improvement methods, the nature of the reaction kinetics limits the radius of tube, assuming cooling occurs on the tube outside only. This implies, combined with other factors, for a large commercial size reactor, a shell & tube reactor is the most viable option for hydride based CSP TCES based on the three approaches discussed in this section. However, there are design considerations with this type of reactor. For shell & tube heat exchangers, adding tubes (equivalent to adding radius) splits the flow rate through the tubes, while also increasing the heat transfer area. For MH shell & tube reactors, adding tubes (equivalent to adding radius) adds more MH reactant, so even though the heat transfer area ($A$) is increased, so is the heat duty ($Q$) of the reactor. To increase the temperature difference between the HTF outlet to inlet ($\Delta T_{HTF}$) (shell side) there are several methods that can be utilized, such as:

- By increasing the reactor length ($L$) at a given shell diameter, due to increasing the shell radius adds a whole set of tubes rather than just extending existing ones, and the HTF has a longer residence time (figure 11(a)).
- By increasing the reactor bed equivalent effective thermal conductivity (figure 10(b)), however this will reduce total reaction time and needs to be considered relative to the convective heat transfer coefficient.
- Decreasing the HTF velocity (or mass flow rate) at a given shell diameter, enabling longer HTF residence time (figure 11(c)). For high pressure gases, an acceptable velocity is between 5 and 10 m s$^{-1}$ [86], although there is argument the velocity could be lower for TCES applications.
- Changing the HTF. This is shown in figure 11(d). The comparison is between carbon dioxide (properties at 400 °C and 10 bar), and helium (properties at 400 °C and 10 bar). Due to the lower density of He, at 10 m s$^{-1}$, the shell pressure drop (nozzle excluded) is 60 Pa, while for CO$_2$ at 10 m s$^{-1}$ the $\Delta P = 5000$ Pa. In general, helium is a superior heat transfer fluid than pressurised CO$_2$, especially considering cost and abundance, but CO$_2$ is sufficient.

The graphs generated in figure 11 are based on a demonstration shell and tube reactor model, with a base case of shell diameter 0.1 m, a tube length of 4.5 m and a tube bundle of six 1″ tubes with a 0.065″ wall thickness. The assumed material is magnesium hydride, using carbon dioxide at 400 °C and 10 bar (property data taken from the NIST Thermophysical Database [87]). The Kern method was adopted to find pressure drops and transfer coefficients [86, 88], with the equations in section 2.1 used for the reaction domain.

**Figure 11.** Illustration of changing the reactor length (a), reactor bed thermal conductivity (b), cross velocity between tube bundle (c), heat transfer fluid (d), and their respective effects on the $\Delta T_{\mathrm{HTF}}$ in comparison to the base case.

### 3.4.2. Reactors in series approach

An interesting outcome from the SAM indicates that a continuous modification in the gas pressure allows for direct control in the fluid outlet temperature. The simulations suggest that the gas pressure can be modified to encourage a flat outlet temperature profile for an adequate time period. By utilising this control mechanism, the outlet of reactor one can be used as the inlet for reactor two to create a reactor in series assembly. This is shown in figure 12, by modifying the shell and tube prototype model shown in the previous section.

In this prototype, the shell diameter = 0.1 m, 5 m tube length, six 1″ tubes with 0.065″ wall thickness, $CO_2$ @ 10 bar as the HTF with velocity 7.5 m s$^{-1}$, fill density of 1.3 g cm$^{-3}$ and $\lambda_{\mathrm{ee}}$ = 4.75 W m$^{-1}$ K$^{-1}$. The total energy is 10 kWh using $MgH_2$ and 80% capture based on the enthalpy of reaction (75 kJ mol$^{-1}$), due to hydrogenation not reaching full theoretical capacity.

Each reactor has individual pressure control, such that in the case illustrated in figure 11, a constant outlet temperature of 8 h is achieved. Assuming the target storage period is 12–14 h, the constant outlet temperature period can be lengthened, and the temperature profile subsequently optimised by the applying the techniques listed earlier. For example, the pressure is controlled to slowly ramp up the reactor during the evening, sustained at a constant temperature overnight, and then ramped down in the morning.
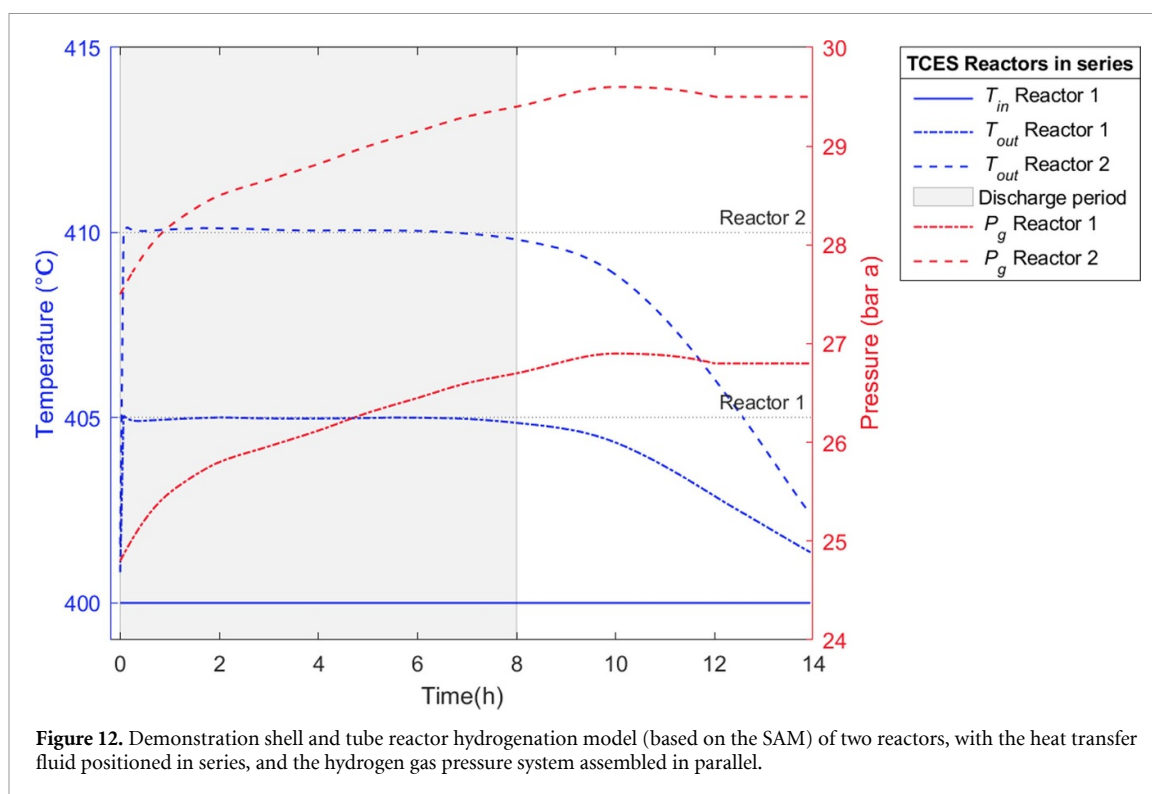
**Figure 12.** Demonstration shell and tube reactor hydrogenation model (based on the SAM) of two reactors, with the heat transfer fluid positioned in series, and the hydrogen gas pressure system assembled in parallel.

Note that a large $\Delta T_{\mathrm{HTF}}$ across one reactor will mean some portions of the bed will encounter much higher over-pressure than another (which usually means a higher initial reaction rate). The over-pressure is the magnitude of gas pressure relative to the equilibrium pressure at a given temperature. For a given material, the equilibrium pressure increases exponentially with higher temperature, so the lower temperature reactors might allow for a larger $\Delta T_{\mathrm{HTF}}$ than the higher temperature reactors. It is then reasonable to explore modifying/changing the material for these higher temperature reactors, which is achievable through the reactors in series approach.

## 4. Thermal stores—scale up

### 4.1. Past prototypes

Past MH TCES prototypes have been developed over the years typically up to 1 kg of material. The size of the prototype determines the amount of energy to be stored, but also defines the quantity of hydrogen gas that must be stored. As such, LTMH have been considered to store hydrogen near room temperature. In either case, a thermocline has been proposed to act as a device to store and release thermal energy from the specific heat of hydrogen gas as it exits and re-enters the high temperature reactor [89]. The operational temperature puts constraints on the containment materials used at high temperature, especially when using hydrogen due to its permeability and embrittlement issues. A critical requirement is to deliver and extract heat to and from all regions of the powder bed, which requires heat extraction, typically via a HTF. Choosing a suitable HTF is reliant on the operating temperature and power requirements of the battery, but usually liquids or high-pressure gases are used [90]. The extraction of heat through the powder bed also requires careful design of the geometry of the powder bed to optimise the rate of extraction/delivery. This has led to numerical modelling studies that have, for example, been undertaken to study the effectiveness of superheated water as a HTF inside of a $MgH_2$ reactor [91, 92]. The air and water sensitive nature of MHs also creates additional concerns and could increase handling, synthesis, and construction costs, which are not a major issue with other thermochemical technologies [24–26].

A 150 g scale thermochemical prototype was recently constructed containing $NaMgH_3$, which showed minimal capacity loss operating over 40 cycles at $\approx$420 °C [93]. This prototype consisted of two cylindrical reactors with internal helical heat exchange tubes containing supercritical water vapour. Despite this geometry, the prototype still suffered issues with uneven heat distribution through the powder bed, resulting in local temperature gradients and thus differences in equilibrium pressures. These problems caused slower kinetics, but also the degradation of the $NaMgH_3$ in some regions, with the unwanted formation of Na metal. The HTF was able to extract heat from the prototype as required, but its effectiveness was limited by
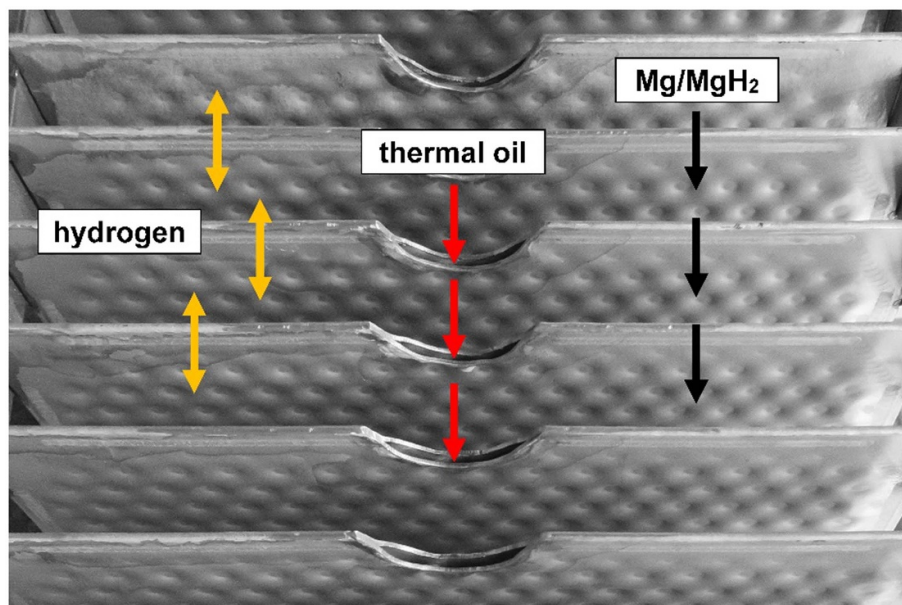
**Figure 13.** Pillow plate heat exchanger (oil distribution system not installed) with thermal oil flow between the embossed plates and Mg/MgH$_2$ between the welded pairs of embossed plates.

the scale of the prototype. The cause is the quantity of MH, which is low compared to the mass of the containment vessel, which also influences the energy storage via its specific heat. More importantly, the thermal losses to the environment through the outer walls of the reactor were significant (more than 30%), despite heavy insulation, due to the high surface to volume ratio of the reactor, also indicated by previous small-scale studies [94].

Insight was gained into the use of an LTMH to store hydrogen gas near room temperature when it was coupled to a high temperature metal hydride (HTMH) such as Mg$_2$FeH$_6$, in a thermal battery prototype [35]. The study utilised 85 g of a titanium manganese alloy (Alloy 5800) as the LTMH (near 20 °C) coupled to 40 g of Mg$_2$FeH$_6$ operating from 350 °C to 500 °C. Ideally, the hydrogen pressure should be controlled by changing the temperature of the LTMH to release or absorb hydrogen gas from the system. This gas pressure would then drive hydrogen absorption or release in the HTMH, causing energy storage or release from the thermal battery. Considerable issues were identified with the performance of the LTMH in this role due to its hysteresis and a 'sloping thermodynamic equilibrium plateau', a result of its changing thermodynamics of hydrogen release as a function of its hydrogen composition. This meant that large swings in temperature or pressure were required in the system to fill the LTMH with hydrogen and allow it to release enough to hydrogenate the HTMH. Despite these issues, the LTMH presented rapid kinetics of reaction, which allowed for responsive energy release/storage in the HTMH.

To address the small-scale issue, a 900 g Mg$_2$FeH$_6$ reactor was assessed as a thermochemical battery [95]. The battery was cycled between 410 °C and 450 °C using a supercritical water HTF and maintained an energy capacity of 1650 kJ, which was 90% of the theoretical capacity. The MH was contained in 8 cylindrical tubes, externally wrapped with HTF tubing, which was used to control the temperature of the high temperature reactor. The hydrogen gas was stored in a 50 l gas bottle through a gas compressor and released back into the reactor via a pressure regulator to provide excellent control and automation over the reaction rate and conditions. 82% of the theoretical energy available was extracted by the HTF after optimisation of the HTF flow and supply pressure. The battery also provided constant power delivery of 39 W to the HTF over an 8-hour window, equating to 1.1 MJ, whereas energy storage was delivered over 12 h at 26 W by the HTF.

### 4.2. Recent prototype development

With MH TCES technology requiring a large step-up, an industry relevant prototype scale is now to be demonstrated in the 'HyHeatStore' project funded by European Union and state of NRW in Germany. Approximately 350 kg of magnesium metal is proposed to store about 200 kWh$_{th}$ in a temperature range between 370 °C and 400 °C.
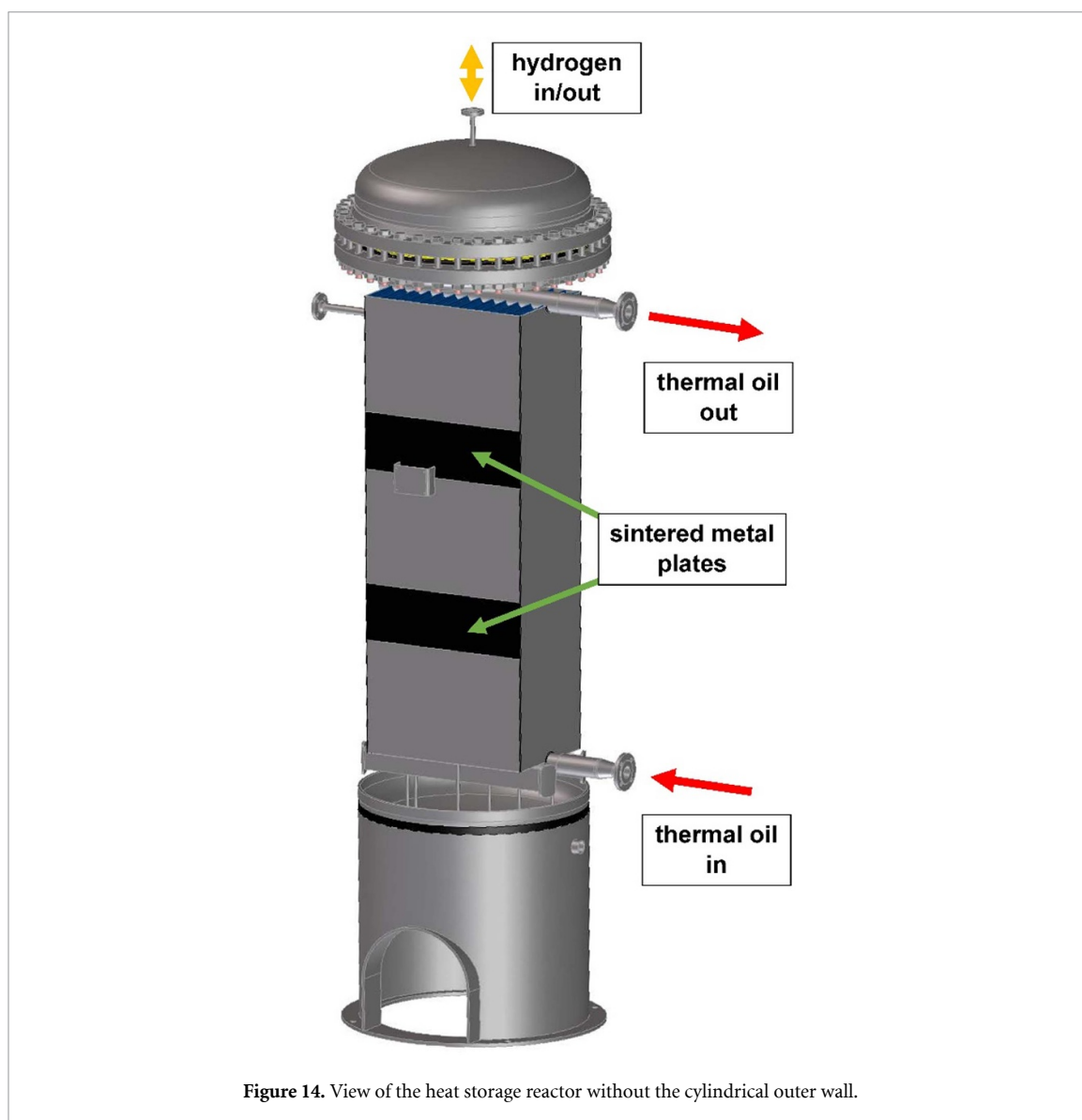
**Figure 14.** View of the heat storage reactor without the cylindrical outer wall.

### 4.2.1. Storage material

The Mg/MgH$_2$ system is one of the most comprehensively studied systems for hydrogen and heat storage and has been investigated in small demonstration plants [37]. The main advantages of this system are the high theoretical hydrogen storage capacity of 7.6 wt% and a heat of reaction of 75 kJ mol$^{-1}$ H$_2$. In practice, storage capacities between 6 and 6.5 wt% of hydrogen are achieved. To improve the kinetics of hydrogen uptake and release, catalysts are added, and the Mg/catalyst mixture is often mixed by ball milling. However, due to the added complexity, this process is only suitable to a limited extent for technical applications. In the HyHeatStore project pure Fe-metal with a particle size of 325 mesh (<44 $\mu$m) is used as the catalyst in an amount of 5 wt%. The Fe-metal powder is mixed with the Mg metal (particle size 325 mesh) by mechanical mixing. This process allows easy, inexpensive, and safe production of magnesium/catalyst mixtures in large quantities.

### 4.2.2. Construction of the storage tank

Normally, as detailed in section 3.4 MH-based reactors are designed and fabricated in a cylindrical shape, either in a single storage vessel or in a tube bundle reactor [96, 97]. However, rectangular plate reactors have also been proposed as vessels for MHs [98–100]. During the exothermic and endothermic reactions occurring from hydrogenation and dehydrogenation of the hydrogen storage metal or alloy, heat must be transferred from or into the reactor in a suitable manner. A very efficient heat exchanger that can be used for heat transfer, is the pillow plate heat exchanger [101]. In this design one fluid flows between two embossed plates (which have the shape of a pillow, figure 13) forming a flow channel and the second fluid flows outside
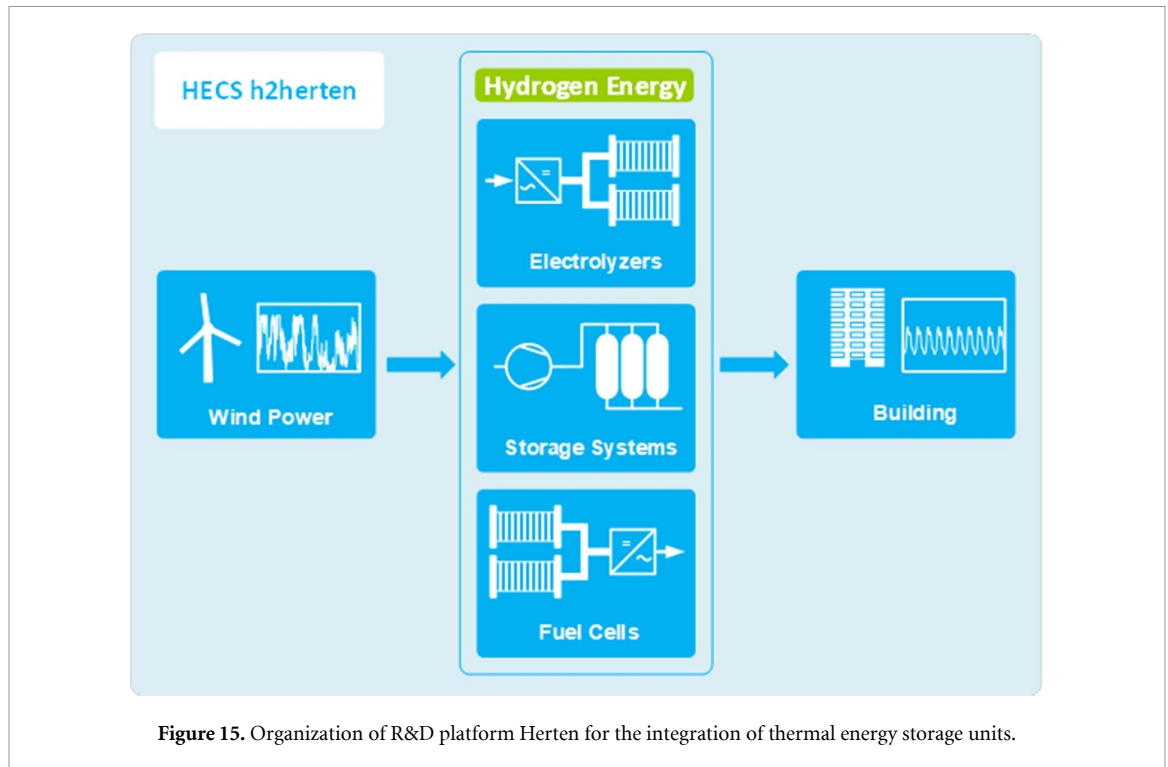
**Figure 15.** Organization of R&D platform Herten for the integration of thermal energy storage units.

the walls of the plates. Various arrangements of the pillow plates can be implemented, which can be combined depending on the desired heat transfer rate. An MH tank with embedded embossed plate heat exchanger has already been numerically simulated for the case of hydrogenation [102]. The reactor design includes 13 embossed and welded plate pairs in the reaction zone, where the HTF flows, while the space between the plate pairs is filled with Mg (3 wt% Fe). The Mg will be hydrogenated to $MgH_2$ during heat release and the $MgH_2$ will be dehydrogenated during heat storage.

The steel used for the reactor is 316 Ti (US ASTM, Werkst.-Nr. 1.4571 EN 10088-2, X6CrNiMoTi 17-12-2 DIN/EN). The thermal oil used for heat transfer is FRAGOLTHERM X-76-A from FRAGOL AG. The maximum distance between the pillow plates is 55 mm (wall thickness of the plates 2.5 mm). The width and height of the plates are 500 and 2000 mm respectively and the heat exchange area is 26 $m^2$. The reactor system is designed for temperatures up to 400 °C, a $H_2$ gas pressure of 25 bar and an oil pressure of 12 bar. The 630 l reactor will be charged with 352 kg of Mg (with 5 wt% Fe) which has a volume of 504 l based on a powder density of $\approx$0.65 g $cm^{-3}$ This leaves sufficient reactor volume for powder expansion during hydrogenation. An oil distributing system is located at the bottom of the pillow plates and an oil collection system at the top.

The box-shaped stack of pillow plates is enclosed by cover plates leaving only the top open for loading the Mg-material. Some of the cover plates are made of sintered metal to allow $H_2$ to flow in- and out of the reaction zone. After infilling the Mg, the powder is prevented from escaping by covering and connecting the rectangular heat exchanger/Mg system with sintered metal plates. The heat exchanger/reaction system covered with plates (solid and sintered) is shown in figure 14, without the outer cylindrical wall. Six thermocouples are provided to measure the temperatures within the reaction chamber.

*4.2.3. System integration*
The integration and demonstration of the heat storage system will take place in an existing $H_2$ infrastructure at the hydrogen competence center h2herten in Herten, Germany. The technological heart of the centre is the hydrogen-based energy supplementation system (HECS—figure 15), a demonstration plant commissioned in 2013 for the 100% renewable energy supply of buildings and technical areas based on hydrogen. It is a hybrid energy storage system consisting of a hydrogen storage unit (max 50 bar) and an additional battery storage unit, enabling the operator to simulate a variety of use cases or scenarios by means of hardware simulation. In the power-to-heat project, existing plant components such as hydrogen storage, ionic compressor, cooling system, a low-voltage switchgear and the necessary feed-in of electrical energy can be used to control and to operate the system.

Figure 16 shows the connection between the heat store system and the periphery. Thermal oil is used as the heat transfer medium, and the system is powered by electricity to simulate the heat input for the power-to-heat system. The exothermic reaction heat inside the reactor can be cooled by h2herten's coolant

**Figure 16.** Schematic view of the heat storage system including the peripheral.
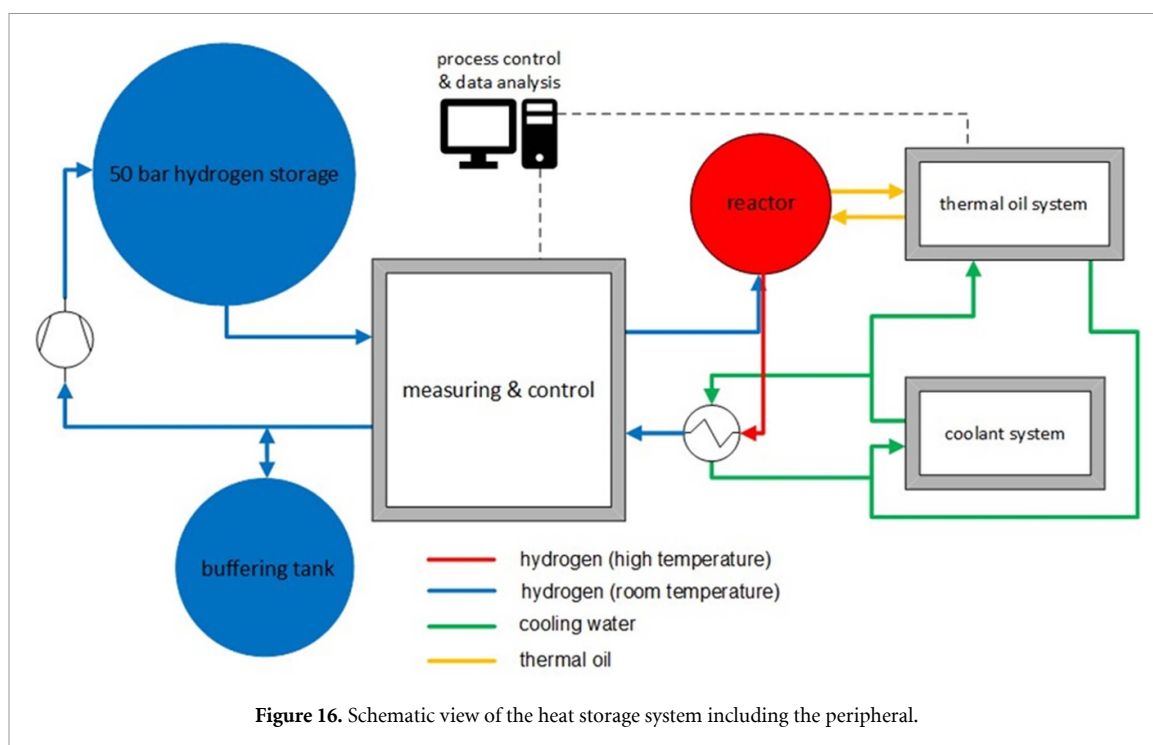
system. The measurement and control section consists of various devices to adjust the flow rate and pressure of hydrogen for the process. Pressure, temperature, and mass flow are measured and transmitted to the process control system for data analysis. The expected hydrogen release rate of the reaction is above the maximum delivery rate of the existing ionic compressor, so that an additional buffer tank had to be installed to temporary store surplus hydrogen. The entire system was designed with a minimum pressure drop so that testing could be performed even if the hydrogen storage unit is not at maximum pressure of 50 bar. The associated process control system provides data recording and trends, control of the thermal oil system, detailed visualization of the key components and an overview of the energy balances during the process. In addition, a program in the form of a simulation for the design and construction of such heat storage systems was developed based on previous experience.

## 5. Conclusion

Here we have discussed the progress in MH TCES specifically targeted for CSP TES. This includes material design and characterization, reactor design from kinetic modelling to engineering considerations, and scale-up developments. We have demonstrated models specifically tailored for MH systems, such as the SAM and mesoscale multi-scale modelling, which can be readily applied to $MgH_2$, a CSP candidate, and potentially to next generation higher temperature MH CSP materials. In addition, several destabilized Ca and Sr systems suitable for 700 °C operation are presented, along with the recommendation of modified sample holder materials for effective material characterization (such as SS coated with aluminum oxide). The effective thermal conductivity of MH systems is an important parameter, where it is outlined that for CSP MH systems hydrogenation $\lambda_e$ is in the range of 0.7–3 W m$^{-2}$ K$^{-1}$, the dehydrogenation $\lambda_e$ is greater than hydrogenation, and the $\lambda_e$ varies with cycle number. Regarding MH TCES reactor design, a shell and tube reactor layout was determined as a technical feasible solution based on established and widespread technology, and the simulations suggest reactors should be positioned in series with pressure control to enable effective management of the HTF temperature. Although a shell & tube reactor is a safe option, other options should be explored, and we also cover the potential for a pillow plate design for MH TCES.

The future target of MH TCES research is to focus on the 700 °C temperature zone. Kinetic models of these 700 °C materials need to be validated and proven, with further refinement and discovery of cost-effective MH TCES materials at 700 °C. The scale-up development should look towards retrofitting current CSP plants to prove the technology (up to 565 °C), while also constructing small-scale reactor demonstrators at 700 °C to help achieve the long-term aim of high temperature CSP plants. With the research community tackling these challenges together, we can realize the potential of MH TCES.

## Data availability statement

## Acknowledgments

## ORCID iDs

Craig E Buckley ⬤ https://orcid.org/0000-0002-3075-1863
Robin Bunzel ⬤ https://orcid.org/0000-0002-0548-4409
Tae Wook Heo ⬤ https://orcid.org/0000-0002-0765-3480
Terry D Humphries ⬤ https://orcid.org/0000-0003-1015-4495
Torben R Jensen ⬤ https://orcid.org/0000-0002-4278-3221
Julian Klug ⬤ https://orcid.org/0000-0003-1618-7490
Kasper T Møller ⬤ https://orcid.org/0000-0002-1970-6703
Mark Paskevicius ⬤ https://orcid.org/0000-0003-2677-3434
Drew A Sheppard ⬤ https://orcid.org/0000-0003-0329-094X
Alastair D Stuart ⬤ https://orcid.org/0000-0002-1886-2560
Robert Urbanczyk ⬤ https://orcid.org/0000-0002-9046-7522
Fei Wang ⬤ https://orcid.org/0000-0002-3798-3974
Gavin S Walker ⬤ https://orcid.org/0000-0001-5038-6923
Brandon C Wood ⬤ https://orcid.org/0000-0002-1450-9719
Danny Weiss ⬤ https://orcid.org/0000-0001-8511-2527
David M Grant ⬤ https://orcid.org/0000-0002-6786-7720

## References

[1] IEA 2020 Solar—key findings (available at: www.iea.org/fuels-and-technologies/solar) (Accessed 15 May 2020)
[2] Laughlin R B 2017 Pumped thermal grid storage with heat exchange *J. Renew. Sustain. Energy* **9** 044103
[3] Steinmann W D, Jockenhöfer H and Bauer D 2020 Thermodynamic analysis of high-temperature carnot battery concepts *Energy Technol.* **8** 1900895
[4] Bott C, Dressel I and Bayer P 2019 State-of-technology review of water-based closed seasonal thermal energy storage systems *Renew. Sustain. Energy Rev.* **113** 109241

[5]   IEA 2014 *Technology Roadmap, Solar Thermal Electricity Plants* (https://doi.org/10.1002/9783527687039.ch06)

[6]   Solargis 2019 Solar resource maps (available at: https://solargis.com/maps-and-gis-data/download) (Accessed 22 October 2019)

[7]   Murphy C, Sun Y, Cole W, Maclaurin G, Turchi C and Mehos M 2019 The potential role of concentrating solar power within the context of DOE's 2030 solar cost targets (available at: www.nrel.gov/docs/fy19osti/71912.pdf)

[8]   Palacios A, Barreneche C, Navarro M E and Ding Y 2020 Thermal energy storage technologies for concentrated solar power—a review from a materials perspective *Renew. Energy* **156** 1244–65

[9]   Mehos M, Turchi C, Vidal J, Wagner M, Ma Z, Ho C, Kolb W, Andraka C, Ma Z and Kruizenga A NREL 2017 *Concentrating Solar Power Gen3 Demonstration Roadmap* (https://doi.org/10.2172/1338899)

[10]  André L, Abanades S and Flamant G 2016 Screening of thermochemical systems based on solid-gas reversible reactions for high temperature solar thermal energy storage *Renew. Sustain. Energy Rev.* **64** 703–15

[11]  Zhou D, Zhao C Y, Tian Y, Lott M C, Kim S-I, Eames P, Loveday D, Haines V and Romanos P (European Commission F. Advantage, N. Term, B. Post, IRENA, ETSAP, and DNV KEMA Energy and Sustainability) 2013 *Thermal Energy Storage, Technology Brief* (available at: https://www.irena.org/publications/2013/Jan/Thermal-energy-storage)

[12]  Lovegrove K and Stein W 2012 Introduction to concentrating solar power (CSP) technology *Concentrating Solar Power Technology* eds K Lovegrove and W Stein (Cambridge: Woodhead Publishing) ch 1, pp 3–15

[13]  Dunn R, Lovegrove K and Burgess G 2012 A review of ammonia-based thermochemical energy storage for concentrating solar power *Proc. IEEE* **100** 391–400

[14]  Bayon A, Bader R, Jafarian M, Fedunik-Hofman L, Sun Y, Hinkley J, Miller S and Lipiński W 2018 Techno-economic assessment of solid–gas thermochemical energy storage systems for solar thermal power applications *Energy* **149** 473–84

[15]  Manickam K *et al* 2019 Future perspectives of thermal energy storage with metal hydrides *Int. J. Hydrog. Energy* **44** 7738–45

[16]  Pardo P, Deydier A, Anxionnaz-Minvielle Z, Rougé S, Cabassud M and Cognet P 2014 A review on high temperature thermochemical heat energy storage *Renew. Sustain. Energy Rev.* **32** 591–610

[17]  Prieto C, Cooper P, Fernández A I and Cabeza L F 2016 Review of technology: thermochemical energy storage for concentrated solar power plants *Renew. Sustain. Energy Rev.* **60** 909–29

[18]  Felderhoff M and Bogdanović B 2009 High temperature metal hydrides as heat storage materials for solar and related applications. *Int. J. Mol. Sci.* **10** 325–44

[19]  Makepeace J W, Wood T J, Hunter H M A, Jones M O and David W I F 2015 Ammonia decomposition catalysis using non-stoichiometric lithium imide *Chem. Sci.* **6** 3805–15

[20]  Block T and Schmücker M 2016 Metal oxides for thermochemical energy storage: a comparison of several metal oxide systems *Sol. Energy* **126** 195–207

[21]  Ortiz C, Valverde J M, Chacartegui R, Pérez-maqueda L A and Gimenez-gavarrell P 2021 Scaling-up the calcium-looping process for $CO_2$ capture and energy storage *KONA Powder and Particle J.* **38** 189–208

[22]  Hanak D P, Anthony E J and Manovic V 2015 A review of developments in pilot-plant testing and modelling of calcium looping process for $CO_2$ capture from power generation systems *Energy Environ. Sci.* **8** 2199–249

[23]  Ortiz C, Valverde J M, Chacartegui R, Perez-Maqueda L A and Giménez P 2019 The calcium-looping ($CaCO_3/CaO$) process for thermochemical energy storage in concentrating solar power plants *Renew. Sustain. Energy Rev.* **113** 109252

[24]  Møller K T, Ibrahim A, Buckley C E and Paskevicius M 2020 Inexpensive thermochemical energy storage utilising additive enhanced limestone *J. Mater. Chem.* A **8** 9646–53

[25]  Møller K T, Williamson K, Buckley C E and Paskevicius M 2020 Thermochemical energy storage properties of a barium based reactive carbonate composite *J. Mater. Chem.* A **8** 10935–42

[26]  Humphries T D, Møller K T, Rickard W D A, Sofianos M V, Liu S, Buckley C E and Paskevicius M 2019 Dolomite: a low cost thermochemical energy storage material *J. Mater. Chem.* A **7** 1206–15

[27]  Zhang K, Li X S, Chen H, Singh P and King D L 2016 Molten salt promoting effect in double salt $CO_2$ absorbents *J. Phys. Chem. C* **120** 1089–96

[28]  Sánchez Jiménez P E, Perejón A, Benítez Guerrero M, Valverde J M, Ortiz C and Pérez Maqueda L A 2019 High-performance and low-cost macroporous calcium oxide based materials for thermochemical energy storage in concentrated solar power plants *Appl. Energy* **235** 543–52

[29]  Sayyah M, Lu Y, Masel R I and Suslick K S 2013 Mechanical activation of CaO-based adsorbents for $CO_2$ capture *ChemSusChem* **6** 193–8

[30]  Takasu H, Ryu J and Kato Y 2017 Application of lithium orthosilicate for high-temperature thermochemical energy storage *Appl. Energy* **193** 74–83

[31]  Møller K, Humphries T D, Berger A, Paskevicius M and Buckley C E 2021 Thermochemical energy storage system development utilising limestone *Chem. Eng. J. Adv.* **8** 100168

[32]  Sheppard D A and Buckley C E 2019 The potential of metal hydrides paired with compressed hydrogen as thermal energy storage for concentrating solar power plants *Int. J. Hydrog. Energy* **44** 9143–63

[33]  Brooks K, Rönnebro E, Simmons A K, Johnson K, Weimar M, Klymyshyn K, Westman M and Pires R 2016 PNNL development and analysis of material-based hydrogen storage systems for the hydrogen storage engineering center of excellence (available at: : https://www.osti.gov/biblio/1330923)

[34]  McClaine A W, Brown K and Bowen D D G 2015 Magnesium hydride slurry: a better answer to hydrogen storage *J. Energy Resour. Technol. Trans. ASME* **137** 6

[35]  Poupin L, Humphries T D, Paskevicius M and Buckley C E 2020 An experimental high temperature thermal battery coupled to a low temperature metal hydride for solar thermal energy storage *Sustain. Energy Fuels* **4** 285–92

[36]  Urbanczyk R, Peinecke K, Peil S and Felderhoff M 2017 Development of a heat storage demonstration unit on the basis of $Mg_2FeH_6$ as heat storage material and molten salt as heat transfer media *Int. J. Hydrog. Energy* **42** 13818–26

[37]  Bogdanović B, Ritter A, Spliethoff B and Straßburger K 1995 A process steam generator based on the high temperature magnesium hydride/magnesium heat storage system *Int. J. Hydrog. Energy* **20** 811–22

[38]  Barkhordarian G, Klassen T and Bormann R 2006 Kinetic investigation of the effect of milling time on the hydrogen sorption reaction of magnesium catalyzed with different $Nb_2O_5$ contents *J. Alloys Compd.* **407** 249–55

[39]  Levenspiel O 1999 *Chemical Reaction Engineering* 3rd edn (New York: Wiley)

[40]  Mintz M H and Zeiri Y 1994 Hydriding kinetics of powders *J. Alloys Compd.* **216** 159–75

[41]  Mintz M H and Bloch J 1983 A kinetic model for hydrogen-metal reactions controlled by a phase transformation step *J. Chem. Phys.* **78** 6569–78

[42] Mintz M H and Bloch J 1985 Evaluation of the kinetics and mechanisms of hybriding reactions *Prog. Solid State Chem.* **16** 163–94

[43] Chou K and Xu K 2007 A new model for hydriding and dehydriding reactions in intermetallics *Intermetallics* **15** 767–77

[44] Ron M 1999 The normalized pressure dependence method for the evaluation of kinetic rates of metal hydride formation/decomposition *J. Alloys Compd.* **283** 178–91

[45] Nasrallah S B and Jemni A 1997 Heat and mass transfer models in metal-hydrogen reactor *Int. J. Hydrog. Energy* **22** 67–76

[46] Jemni A, Ben Nasrallah S and Lamloumi J 1999 Experimental and theoretical study of a metal-hydrogen reactor *Int. J. Hydrog. Energy* **24** 631–44

[47] Chaise A, De Rango P, Marty P and Fruchart D 2010 Experimental and numerical study of a magnesium hydride tank *Int. J. Hydrog. Energy* **35** 6311–22

[48] Mayer U, Groll M and Supper W 1987 Heat and mass transfer in metal hydride reaction beds: experimental and theoretical results *J. Less Common Met.* **131** 235–44

[49] Herbrig K, Röntzsch L, Pohlmann C, Weißgärber T and Kieback B 2013 Hydrogen storage systems based on hydride–graphite composites: computer simulation and experimental validation *Int. J. Hydrog. Energy* **38** 7026–36

[50] Ley M B, Meggouh M, Moury R, Peinecke K and Felderhoff M 2015 Development of hydrogen storage tank systems based on complex metal hydrides *Materials* **8** 5891–921

[51] Ahluwalia R K 2007 Sodium alanate hydrogen storage system for automotive fuel cells *Int. J. Hydrog. Energy* **32** 1251–61

[52] Mellouli S, Dhaou H, Askri F, Jemni A and Ben Nasrallah S 2009 Hydrogen storage in metal hydride tanks equipped with metal foam heat exchanger *Int. J. Hydrog. Energy* **34** 9393–401

[53] Souahlia A, Dhaou H, Mellouli S, Askri F, Jemni A and Ben Nasrallah S 2014 Experimental study of metal hydride-based hydrogen storage tank at constant supply pressure *Int. J. Hydrog. Energy* **39** 7365–72

[54] Adams M, Grant D M, Stuart A and Walker G S 2019 Modelling a kinetic deviation of the magnesium hydrogenation reaction at conditions close to equilibrium *Int. J. Hydrog. Energy* **44** 29123–31

[55] Adams M 2021 Design and Operation of a Metal Hydride Reactor within a Thermochemical Energy Store for Use in Concentrated Solar Power *Thesis (PhD)* University of Nottingham

[56] El Maakoul A, Laknizi A, Saadeddine S, Ben Abdellah A, Meziane M and El Metoui M 2017 Numerical design and investigation of heat transfer enhancement and performance for an annulus with continuous helical baffles in a double-pipe heat exchanger *Energy Convers. Manage.* **133** 76–86

[57] Kim D, Han D J, Heo T W, Kang S, Wood B, Lee J, Cho E S and Lee B J 2022 Enhancement of effective thermal conductivity of rGO/Mg nanocomposite packed beds *Int. J. Heat Mass Transfer* **192** 122891

[58] Heo T W, Bhattacharyya S and Chen L Q 2013 A phase-field model for elastically anisotropic polycrystalline binary solid solutions *Phil. Mag.* **93** 1468–89

[59] Heo T W and Chen L Q 2014 Phase-field modeling of displacive phase transformations in elastically anisotropic and inhomogeneous polycrystals *Acta Mater.* **76** 68–81

[60] Heo T W, Colas K B, Motta A T and Chen L Q 2019 A phase-field model for hydride formation in polycrystalline metals: application to δ-hydride in zirconium alloys *Acta Mater.* **181** 262–77

[61] Møller K T, Jensen T R, Akiba E and Li H-W 2017 Hydrogen—a sustainable energy carrier *Prog. Nat. Sci. Mater. Int.* **27** 34–40

[62] Tortoza M S, Humphries T D, Sheppard D A, Paskevicius M, Rowles M R, Sofianos M V, Aguey-Zinsou K F and Buckley C E 2018 Thermodynamics and performance of the Mg-H-F system for thermochemical energy storage applications *Phys. Chem. Chem. Phys.* **20** 2274–83

[63] Paskevicius M, Sheppard D A and Buckley C E 2010 Thermodynamic changes in mechanochemically synthesized magnesium hydride nanoparticles *J. Am. Chem. Soc.* **132** 5077–83

[64] Griffond A C M, Sofianos M V, Sheppard D A, Humphries T D, Sargent A L, Dornheim M, Aguey-Zinsou K F and Buckley C E 2021 High-temperature thermochemical energy storage using metal hydrides: destabilisation of calcium hydride with silicon *J. Alloys Compd.* **858** 158229

[65] Sofianos M V, Randall S, Paskevicius M, Aguey-Zinsou K F, Rowles M R, Humphries T D and Buckley C E 2020 Exploring halide destabilised calcium hydride as a high-temperature thermal battery *J. Alloys Compd.* **819** 153340

[66] Balakrishnan S, Sofianos M V, Humphries T D, Paskevicius M and Buckley C E 2020 Thermochemical energy storage performance of zinc destabilized calcium hydride at high-temperatures *Phys. Chem. Chem. Phys.* **22** 25780–8

[67] Balakrishnan S, Sofianos M V, Paskevicius M, Rowles M R and Buckley C E 2020 Destabilized calcium hydride as a promising high-temperature thermal battery *J. Phys. Chem.* C **124** 17512–9

[68] Peterson D T 1980 Equilibrium hydrogen pressures in the strontium-hydrogen system *J. Less Common Met.* **72** 251–6

[69] Humphries T D, Paskevicius M, Alamri A and Buckley C E 2022 Thermodynamic destabilisation of SrH$_2$ using Al for the next generation of high temperature thermal batteries *J. Alloys Compd.* **894** 162404

[70] Ward P A, Teprovich J A, Liu Y, He J and Zidan R 2018 High temperature thermal energy storage in the CaAl$_2$ system *J. Alloys Compd.* **735** 2611–5

[71] Kim S T, Kurahashi C, Hoshino H, Takahashi C, Tamura Y, Takasu H, Saito S, Kurihara M and Kato Y 2019 Thermal driving demonstration of Li$_4$SiO$_4$/CO$_2$/zeolite thermochemical energy storage system for efficient high-temperature heat utilizations *ISIJ Int.* **59** 721–6

[72] Humphries T D, Sheppard D A, Rowles M R, Sofianos M V and Buckley C E 2016 Fluoride substitution in sodium hydride for thermal energy storage applications *J. Mater. Chem.* A **4** 12170–8

[73] Sheppard D A, Corgnale C, Hardy B, Motyka T, Zidan R, Paskevicius M and Buckley C E 2014 Hydriding characteristics of NaMgH$_2$F with preliminary technical and cost evaluation of magnesium-based metal hydride materials for concentrating solar power thermal storage *RSC Adv.* **4** 26552–62

[74] Sheppard D A, Humphries T D and Buckley C E 2016 Sodium-based hydrides for thermal energy applications *Appl. Phys.* A **122** 406

[75] Humphries T D, Rawal A, Rowles M R, Prause C R, Bird J E, Paskevicius M, Sofianos M V and Buckley C E 2020 Physicochemical characterization of a Na-H-F thermal battery material *J. Phys. Chem.* C **124** 5053–60

[76] Humphries T D, Yang J, Mole R A, Paskevicius M, Bird J E, Rowles M R, Tortoza M S, Veronica Sofianos M, Yu D and Buckley C E 2020 Fluorine substitution in magnesium hydride as a tool for thermodynamic control *J. Phys. Chem.* C **124** 9109–17

[77] Sheppard D A, Paskevicius M, Javadian P, Davies I J and Buckley C E 2019 Methods for accurate high-temperature sieverts-type hydrogen measurements of metal hydrides *J. Alloys Compd.* **787** 1225–37

[78] Gray E M A and Webb C J 2020 Metal-hydride hydrogen compressors for laboratory use *J. Phys. Energy* **2** 3

[79] Albert R, Urbanczyk R and Felderhoff M 2019 Thermal conductivity measurements of magnesium hydride powder beds under operating conditions for heat storage applications *Int. J. Hydrog. Energy* **44** 29273–81

[80] Albert R, Wagner C, Urbanczyk R and Felderhoff M 2020 Cycle stability of the effective thermal conductivity of nickel-activated magnesium hydride powder under operating conditions *Energy Technol.* **8** 2000356

[81] Bird J E, Humphries T D, Paskevicius M, Poupin L and Buckley C E 2020 Thermal properties of thermochemical heat storage materials *Phys. Chem. Chem. Phys.* **22** 4617–25

[82] Nitsche M and Gbadamosi R O 2016 Chapter 11 - Double pipe, helical coil, and cross flow heat exchanger *Heat Exchanger Design Guide* 1st edn (Oxford: Butterworth-Heinemann) pp 229–45

[83] Ron M, Gruen D, Mendelsohn M and Sheet I 1980 Preparation and properties of porous metal hydride compacts *J. Less Common Met.* **74** 445–8

[84] Kim K J, Montoya B, Razani A and Lee K-H 2001 Metal hydride compacts of improved thermal conductivity *Int. J. Hydrog. Energy* **26** 609–13

[85] Dieterich M, Pohlmann C, Bürger I, Linder M and Röntzsch L 2015 Long-term cycle stability of metal hydride-graphite composites *Int. J. Hydrog. Energy* **40** 16375–82

[86] Sinnott R K 2005 *Coulson and Richardson's Chemical Engineering Volume 6—Chemical Engineering Design* 4th edn (Oxford: Butterworth-Heinemann)

[87] Lemmon E W and McLinden M O 2001 NIST standard reference database 23: NIST reference fluid thermodynamic and transport properties (Gaithersburg: National Institute of Standards and Technology)

[88] Coulson J M, Backhurst J R and Harker J H 1999 *Coulson and Richardson's Chemical Engineering - Fluid Flow, Heat Transfer and Mass Transfer* 6th edn, vol 1 (Oxford: Butterworth-Heinemann)

[89] Harries D N, Paskevicius M, Sheppard D A, Price T E C and Buckley C E 2011 Concentrating solar thermal heat storage using metal hydrides *Proc. IEEE* **100** 539–49

[90] Carrillo A J, González-Aguilar J, Romero M and Coronado J M 2019 Solar energy on demand: a review on high temperature thermochemical heat storage systems and materials *Chem. Rev.* **119** 4777–816

[91] Mathew A, Nadim N, Chandratilleke T T, Humphries T D and Buckley C E 2021 Investigation of boiling heat transfer for improved performance of metal hydride thermal energy storage *Int. J. Hydrog. Energy* **46** 28200–13

[92] Mathew A, Nadim N, Chandratilleke T T, Humphries T D, Paskevicius M and Buckley C E 2021 Performance analysis of a high-temperature magnesium hydride reactor tank with a helical coil heat exchanger for thermal storage *Int. J. Hydrog. Energy* **46** 1038–55

[93] Poupin L, Humphries T D, Paskevicius M and Buckley C E 2019 A thermal energy storage prototype using sodium magnesium hydride *Sustain. Energy Fuels* **3** 985–95

[94] Paskevicius M, Sheppard D A, Williamson K and Buckley C E 2015 Metal hydride thermal heat storage prototype for concentrating solar thermal power *Energy* **88** 469–77

[95] Poupin L, Humphries T D T D, Paskevicius M, Buckley C E C E, Møller K, Humphries T D T D, Berger A, Paskevicius M and Buckley C E C E 2021 An operational high temperature thermal energy storage system using magnesium iron hydride *Int. J. Hydrog. Energy* **46** 38755–67

[96] Na Ranong C, Höhne M, Franzen J, Hapke J, Fieg G, Dornheim M, Eigen N, Bellosta von Colbe J M and Metz O 2009 Concept, design and manufacture of a prototype hydrogen storage tank based on sodium alanate *Chem. Eng. Technol.* **32** 1154–63

[97] Garrier S, Chaise A, De Rango P, Marty P, Delhomme B, Fruchart D and Miraglia S 2011 MgH₂ intermediate scale tank tests under various experimental conditions *Int. J. Hydrog. Energy* **36** 9719–26

[98] Gkanas E I, Statheros T and Khzouz M 2019 Heat management on rectangular metal hydride tanks for green building applications *Int. J. Hydrog. Energy* **44** 19267–74

[99] Botzung M, Chaudourne S, Gillia O, Perret C, Latroche M, Percheron-Guegan A and Marty P 2008 Simulation and experimental validation of a hydrogen storage tank with metal hydrides *Int. J. Hydrog. Energy* **33** 98–104

[100] Weckerle C, Bürger I and Linder M 2017 Novel reactor design for metal hydride cooling systems *Int. J. Hydrog. Energy* **42** 8063–74

[101] Zibart A and Kenig E Y 2021 Numerical investigation of conjugate heat transfer in a pillow-plate heat exchanger *Int. J. Heat Mass Transfer* **165** 120567

[102] Lewis S D and Chippar P 2020 Numerical investigation of hydrogen absorption in a metal hydride reactor with embedded embossed plate heat exchanger *Energy* **194** 116942